The microtubule- and PP1-binding activities of *Drosophila melanogaster* Spc105 control the kinetics of SAC satisfaction

Margaux R. Audett[a,b], Erin L. Johnson[a], Jessica M. McGory[a,b], Dylan M. Barcelos[a],
Evelin Oroszne Szalai[c], Marcin R. Przewloka[c], and Thomas J. Maresca[a,b,*]
[a]Biology Department and [b]Molecular and Cellular Biology Graduate Program, University of Massachusetts,
Amherst, Amherst MA 01003; [c]Institute for Life Sciences, School of Biological Sciences, University of Southampton,
Southampton SO17 1BJ, UK

ABSTRACT KNL1 is a large intrinsically disordered kinetochore (KT) protein that recruits spindle assembly checkpoint (SAC) components to mediate SAC signaling. The N-terminal region (NTR) of KNL1 possesses two activities that have been implicated in SAC silencing: microtubule (MT) binding and protein phosphatase 1 (PP1) recruitment. The NTR of *Drosophila melanogaster* KNL1 (Spc105) has never been shown to bind MTs or to recruit PP1. Furthermore, the phosphoregulatory mechanisms known to control SAC protein binding to KNL1 orthologues is absent in *D. melanogaster*. Here, these apparent discrepancies are resolved using in vitro and cell-based assays. A phosphoregulatory circuit that utilizes Aurora B kinase promotes SAC protein binding to the central disordered region of Spc105 while the NTR binds directly to MTs in vitro and recruits PP1-87B to KTs in vivo. Live-cell assays employing an optogenetic oligomerization tag and deletion/chimera mutants are used to define the interplay of MT and PP1 binding by Spc105 and the relative contributions of both activities to the kinetics of SAC satisfaction.

INTRODUCTION

Accurate chromosome segregation is necessary to maintain genomic integrity through cell division. The spindle assembly checkpoint (SAC) is a chemical signal that delays anaphase onset until every pair of chromosomes is properly attached and aligned within the spindle (Musacchio, 2015). Once all chromosomes are bioriented, or properly attached to microtubules (MTs) emanating from opposite spindle poles, the SAC signal is extinguished, and

sister chromatids can physically separate. MT attachment and SAC regulation are mediated by a multiprotein complex called the kinetochore (KT) that assembles at centromeres during cell division (Cheeseman, 2014; Musacchio and Desai, 2017). Structural KT proteins, which are stably maintained at centromeres throughout cell division, are essential to both the attachment and SAC regulatory functions because they possess MT- and checkpoint protein–binding activities. Unlike the stable KT constituents, checkpoint proteins, which associate with KTs in a highly dynamic manner, are abundant at unattached KTs and become diminished as KTs establish end-on attachments to MTs and biorient (Hoffman *et al.*, 2001; Howell *et al.*, 2004; Kuhn and Dumont, 2017). The KT is the physical locale where checkpoint proteins become enriched and posttranslationally modified to promote assembly of a diffusible mitotic checkpoint complex (MCC) that acts as a wait-anaphase signal through inhibition of the anaphase-promoting complex/cyclosome (APC/C) (Sudakin *et al.*, 2001; Alfieri *et al.*, 2016; Yamaguchi *et al.*, 2016). When checkpoint proteins are depleted from bioriented KTs, they cease to produce the wait-anaphase signal, but it remains unclear precisely how the kinetochore-microtubule (KT-MT) attachment state is translated into reduced checkpoint protein–binding affinities and, consequently, SAC satisfaction.

No protein better exemplifies how the KT lies at the nexus of MT attachment and SAC regulation than KNL1 (D40/AF15q14/Blinkin/KNL1/Spc105/CASC5) (Wei *et al.*, 1999; Hayette *et al.*, 2000; Desai *et al.*, 2003; Nekrasov *et al.*, 2003; Kiyomitsu *et al.*, 2007; Genin *et al.*, 2012), which was deemed dmSpc105R (referred to hereafter as Spc105) in *Drosophila melanogaster* (Przewloka *et al.*, 2007). KNL1 is the largest component of the KMN network; an outer KT complex consisting of <u>K</u>NL1, the <u>M</u>is12 complex, and the <u>N</u>dc80 complex (Cheeseman *et al.*, 2006). KNL1 is predicted to be highly disordered except for conserved tandem RWD domains in its C-terminus that anchor it to the outer KT via physical interactions with the Mis12 complex (Petrovic *et al.*, 2010, 2014). Its large size and disordered nature make KNL1 energetically expensive relative to a small, well-folded protein that could, in theory, mediate the same functions. While KNL1 orthologues are highly divergent at the amino acid level, the large size and unstructured nature are well-conserved, indicating that these features are essential for its function.

Work in multiple model systems has shown that KNL1 orthologues bind MTs (Welburn *et al.*, 2010; Roy *et al.*, 2019) via a MT-binding patch located at the extreme N-terminus (Cheeseman *et al.*, 2006; Kerres *et al.*, 2007; Pagliuca *et al.*, 2009; Espeut *et al.*, 2012). While conserved, the function(s) of MT binding by KNL1 is poorly understood. In addition, the N-terminus of KNL1 possesses two well-conserved protein phosphatase 1 (PP1)-binding "SILK" and "RRVSF" motifs (Hendrickx *et al.*, 2009; Liu *et al.*, 2010; Meadows *et al.*, 2011; Rosenberg *et al.*, 2011; Espeut *et al.*, 2012; London *et al.*, 2012; Shepperd *et al.*, 2012; Bajaj *et al.*, 2018). The recruitment of PP1 to KNL1 is phosphoregulated by Aurora B kinase (ABK), which negatively regulates PP1 binding to the two motifs (Liu *et al.*, 2010; Bajaj *et al.*, 2018; Nasa *et al.*, 2018). During the process of biorientation, enzyme dominance must shift from ABK to PP1, but it is unclear how this is accomplished. It is also unclear how MT binding by KNL1 impacts PP1 recruitment in vivo although the interaction of human KNL1 with PP1 and MTs was recently shown to be mutually exclusive in vitro (Bajaj *et al.*, 2018).

The middle region of KNL1 orthologues contains a large array of so-called MELT motifs that recruit multiple checkpoint proteins (BubR1, Bub1, Bub3, Mad1, and Mad2) through direct binding to the checkpoint protein Bub3. The interaction between MELT motifs and Bub3 is highly phosphoregulated by a balance of localized phosphatase and kinase activities. Recruitment of PP1 to the N-terminus of KNL1 promotes dephosphorylation of the MELT motifs, although the precise mechanism is unclear as PP1 does not directly dephosphorylate MELT motifs (Cordeiro *et al.*, 2020). Nonetheless, the KNL1-bound population of PP1 is a key contributor to SAC satisfaction (Meadows *et al.*, 2011; Rosenberg *et al.*, 2011; Espeut *et al.*, 2012; Nijenhuis *et al.*, 2014; Roy *et al.*, 2019) most likely through reducing the affinity of Bub3 for KNL1. In many organisms the checkpoint kinase monopolar spindle 1 (Mps1) generates phosphorylated MELT motifs that exhibit higher-affinity association with Bub3 and support its recruitment to unattached KTs in cells (Pagliuca *et al.*, 2009; Krenn *et al.*, 2012, 2014; London *et al.*, 2012; Shepperd *et al.*, 2012; Yamagishi *et al.*, 2012; Primorac *et al.*, 2013; Vleugel *et al.*, 2013; Zhang *et al.*, 2014). However, Mps1-mediated phosphorylation of MELTs is not a universally conserved mechanism as MELT motifs in *Caenorhabditis elegans* are phosphorylated by Polo-like kinase 1 (PLK1) (Espeut *et al.*, 2015), which has also been implicated in phosphorylating MELT motifs in human cells (Ikeda and Tanaka, 2017; Cordeiro *et al.*, 2020). Surprisingly, Mps1 is dispensable for Bub3 localization to unattached KTs in *Drosophila* S2 cells (Conde *et al.*, 2013). Thus, if Bub3 binds to Spc105, then it occurs independent of phosphoregulation or is promoted by a different kinase in flies.

RESULTS

The Spc105-Bub3 interaction is phosphoregulated by ABK in *Drosophila melanogaster*

Spc105 contains divergent "MELT-like" Bub3-binding motifs with the consensus sequence EP[M/I]EE[E/D] (Tromer *et al.*, 2015)—referred to hereafter as "MEED" motifs. MEED motifs have a phosphomimetic quality because the conserved serine/threonine residues in conventional MELT motifs are replaced by acidic residues. Because Mps1 is dispensable for Bub3 localization to unattached KTs in *Drosophila melanogaster* S2 cells (Conde *et al.*, 2013) and the MEED motif regions have acidic and hydrophobic properties reminiscent of the PLK1 consensus motif (Nakajima *et al.*, 2003), we tested whether PLK1 (POLO in *Drosophila*) activity was required for Bub3 recruitment to unattached KTs in S2 cells. Cells coexpressing Spc105-EGFP and Bub3-TagRFP-T were treated with colchicine to generate unattached KTs and MG132 to maintain a mitotic state. Cells with Bub3 at unattached KTs were visualized via two-color, time-lapse confocal microscopy while introducing the PLK1 inhibitor BI 2536 (Lénárt *et al.*, 2007; Steegmaier *et al.*, 2007), which inhibits POLO activity in S2 cells as evidenced by rapid changes in metaphase spindle morphology (Supplemental Figure S1A and Supplemental Video 1). Inhibition of POLO did not result in a statistically significant reduction in Bub3 levels at KTs (Supplemental Figure S1, B–D, and Supplemental Video 2), revealing that POLO kinase activity is not a major contributor to Bub3 recruitment to unattached KTs in *Drosophila* S2 cells.

Because a putative Aurora kinase motif (Cheeseman *et al.*, 2002) lies upstream of nearly every MEED motif in Spc105 (Schittenhelm *et al.*, 2009; Vleugel *et al.*, 2013; Tromer *et al.*, 2015), we next investigated the contribution of ABK activity to Bub3 localization at unattached KTs. Addition of the *Drosophila* ABK-specific inhibitor Binucleine 2 (Eggert *et al.*, 2004; Smurnyy *et al.*, 2010) resulted in a rapid and significant (>80%) reduction of Bub3 from unattached KTs (Figure 1, A and B, Supplemental Figure S1E, and Supplemental Videos 3 and 4). Thus, ABK activity is required for a significant majority of Bub3 binding to unattached KTs in *Drosophila* S2 cells.

To directly test whether Spc105 is a bona fide substrate of Aurora kinase, in vitro kinase assays were conducted with budding yeast Ipl1 (Aurora kinase orthologue) and a purified portion of Spc105 containing 10 MEED motifs (10xMEED) each of which was preceded by a putative Aurora kinase consensus motif (Figure 1C and Supplemental Figure S1F). Incubation of the 10xMEED with ATP and purified Ipl1, which was hyperactivated through fusion with the Sli15 (budding yeast INCENP) INBOX (gift of the Biggins lab), yielded an evident shift on an SDS–PAGE gel compared with unphosphorylated control samples (Figure 1D). Importantly, the slower mobility of Spc105 was abrogated in the presence of alkaline phosphatase, demonstrating that the observed shift was due to Aurora kinase–mediated phosphorylation.

Pull-down assays using purified Bub3-EGFP and either MBP-TST–tagged 10xMEED or MBP-TST control protein were conducted to determine whether Spc105 and Bub3 directly interact and whether phosphorylation increases their binding affinity (Supplemental Figure S1F). In the absence of phosphorylation, approximately twofold more Bub3 bound to the 10xMEED than to the MBP-TST control (*n* = 3 independent experiments) (Figure 1E). The binding affinity was significantly increased upon phosphorylation of Spc105 as the addition of ATP and activated Sli15-Ipl1 resulted in an ~30-fold increase in Bub3 binding to the 10xMEED compared with the unphosphorylated MBP-TST (*n* = 3 independent experiments) (Figure 1E).
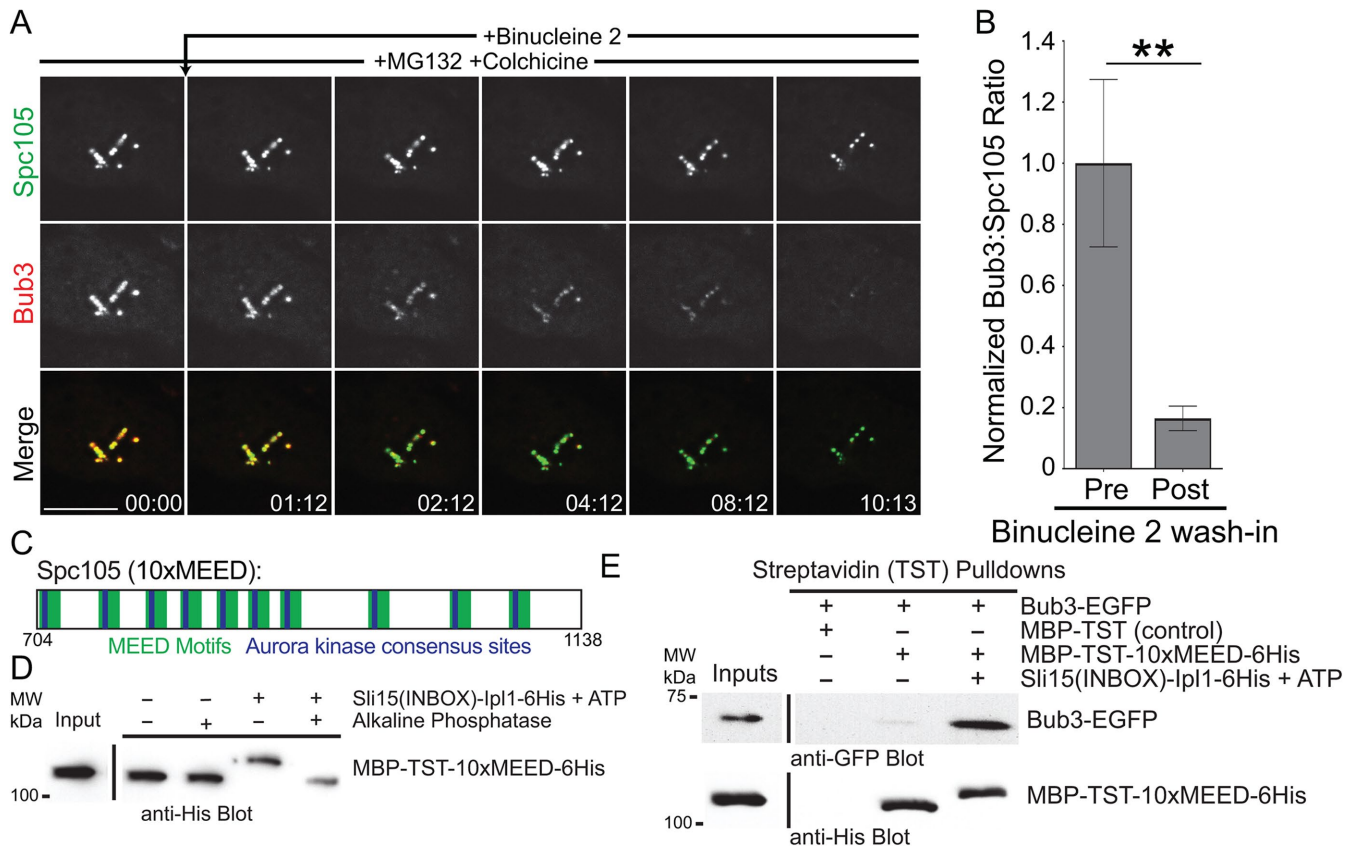
FIGURE 1: ABK phosphoregulates the Bub3-Spc105 interaction. (A) Still frames from spinning-disk confocal time-lapse imaging of a cell coexpressing Spc105-EGFP (green) and Bub3-TagRFP-T (red) treated with MG132 (10 μM) and colchicine (25 μM). The ABK inhibitor Binucleine 2 (40 μM) was added to the imaging chamber ~1 min into the time lapse. (B) Quantification of Bub3 signal ratioed to Spc105 signal intensity pre- and post-Binucleine 2 treatment in wash-in experiments ($n = 8$ cells for pre–wash-in; $n = 12$ cells for post–wash-in). (C) Schematic of Spc105 (10xMEED). (D) Western blot of in vitro kinase assay reactions showing a pronounced shift in the migration of 10xMEED in the presence of activated Sli15(INBOX)-Ipl1. (E) Western blots for GFP (top panel) and the His tag (bottom panel) of pull downs showing that Bub3 interacts with 10xMEED and, to a much greater extent, with phospho-10xMEED, but not with MBP-TST. Displayed times are minutes:seconds. Scale bar is 10 μm. Error bars are SEM. The reported p value was generated by a randomization method: ** p value < 0.005.

Characterization of the MT-binding activity of Spc105

Because Spc105 binding to MTs has not been demonstrated before, we next investigated whether the NTR of Spc105 binds directly to MTs in vitro. There are two isoforms of Spc105 in *D. melanogaster*: Spc105-A and Spc105-B, which differ only in the first nine amino acids such that Spc105-B possesses the conserved N-terminal MT-binding patch while Spc105-A does not (Figure 2A). MT-binding activities of the Spc105 orthologues in yeast and worms were previously investigated using a microscopy-based assay where Spc105 or KNL-1 was coupled to polystyrene beads and incubated with Taxol-stabilized MTs (Espeut *et al.*, 2012; Roy *et al.*, 2019). Aiming to better control the binding conditions, we planned to conduct total internal reflection fluorescence (TIRF)-based imaging assays with purified protein in the absence of polystyrene beads; however, the N-terminus of Spc105 was insoluble by conventional purification methods. The addition of N-terminal solubility tags such as superfolder GFP and MBP conferred solubility, but the protein was insoluble after cleavage of the tags (unpublished observation). Protein solubility of intrinsically disordered proteins (IDPs), which are highly susceptible to proteolysis and aggregation, had previously been maintained using purification buffers supplemented with arginine (Boke *et al.*, 2016). Indeed, soluble Spc105 variants were success-

fully purified in the presence of 500 mM arginine that was subsequently diluted to a final concentration of 100 mM arginine, which did not compromise Spc105 solubility, for use in TIRF-based MT-binding assays (Supplemental Figure S2, A and B).

Spc105-B(1-400)-EGFP bound robustly to Taxol-stabilized MTs in vitro at 50 nM concentration and could be readily detected on MTs at concentrations as low as 10 nM (unpublished observation). To assess binding efficiencies of the Spc105 variants (A vs. B), a final concentration of 50 nM of each EGFP-tagged Spc105 variant or MBP-GFP (control) was incubated with Cy5-labeled Taxol-stabilized MTs in imaging chambers and visualized by TIRF microscopy (Figure 2B). Binding was quantified by measuring the background-corrected fluorescence intensity of the EGFP signal per micron of MT for each Spc105 variant and, for comparison, the data were normalized against Spc105-B(1-400). Spc105-A(1-400), which lacks the basic patch at the immediate N-terminus, bound MTs with significantly reduced efficiency (<50%) compared with Spc105-B(1-400) (Figure 2C). Thus, the basic binding patch at the immediate N-terminus of Spc105-B makes an important contribution to the MT-binding affinity of Spc105 although additional MT-binding sites must be located at the N-terminus because Spc105-A(1-400) still associated with MTs albeit with reduced capacity.
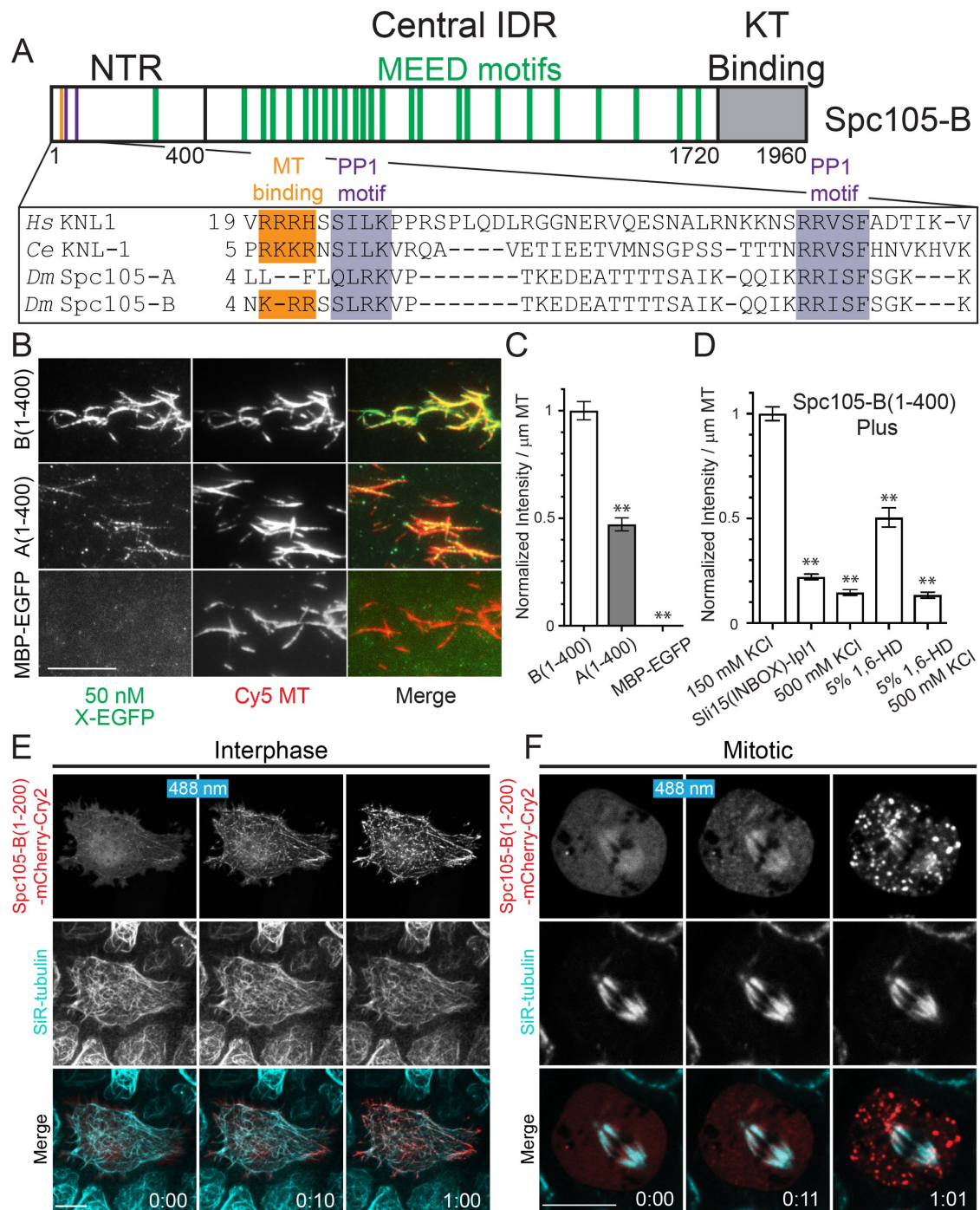
FIGURE 2: Characterization of MT binding by the NTR of Spc105. (A) Schematic of *D. melanogaster* Spc105 highlighting the N-terminal region (NTR) and its alignment with conserved MT-binding and PP1-binding motifs (*Hs: Homo sapiens; Ce: C. elegans; Dm: D. melanogaster*). (B) Representative images of in vitro TIRF assays with Taxol-stabilized Cy5-labeled MTs (red) plus 50 nM of the indicated Spc105-EGFP (green) variant. (C) Quantification of the background-corrected intensity of each Spc105 protein (at 50 nM concentration) per micron of MT normalized to Spc105-B(1-400) ($n = 150$ MTs per Spc105 fragment from three independent experiments; $n = 25$ MTs from one experiment for MBP-EGFP). (D) Intensity quantifications of 50 nM Spc105-B(1-400) per micron of MT under variable binding conditions normalized to Spc105-B(1-400) in 150 mM KCl ($n = 150$ MTs for 150 mM KCl, +Sli15(INBOX)-Ipl1, and 500 mM KCl conditions from three independent experiments; $n = 75$ MTs for 5% 1,6-HD and 5% 1,6-HD + 500 mM KCl from three independent experiments). (E, F) Representative still frames from spinning-disk confocal time-lapse imaging of an interphase (E) or mitotic (F) cell expressing Spc105-B(1-200)-mCherry-Cry2 (red) with the MTs labeled in far-red with SiR-tubulin (cyan). Photo-oligomerization was triggered with a single pulse of 488 nm laser light after the preactivation image was taken at 0:00 in E and F. Displayed times are minutes:seconds. Scale bars are 10 μm. Error bars are SEM. The reported *p* values were generated by a randomization method: ** *p* value < 0.005 for pair-wise comparisons to the B(1-400) in C and the 150 mM KCl in D.

We next focused on altering the experimental conditions of the binding assay using Spc105-B(1-400) to further dissect the nature of how Spc105 interacts with MTs (Figure 2D). We first examined the contribution of electrostatic interactions by repeating the MT-binding assay in the presence of high salt (500 mM KCl), which reduced binding of Spc105-B(1-400) by ~85%. It is well established that electrostatic interactions between basic MT-binding patches and negatively charged MTs can be disrupted by phosphorylation. Spc105-B(1-400) contains multiple Aurora kinase consensus sites in the NTR and phosphomimetic mutants of the Aurora sites in human and worm KNL1 abolished MT binding in cosedimentation assays (Welburn *et al.*, 2010). In agreement with this finding, we found that phosphorylation with Sli15-Ipl1, which resulted in an observable shift in Spc105-B(1-400) on an SDS–PAGE gel (Supplemental Figure S2C), reduced MT binding of Spc105-B(1-400) (22.1%) to nearly the same extent as the high-salt condition (14.6%).

Because Spc105-B(1-400) possesses multiple hydrophobic patches, we next performed MT-binding assays in the presence of 5% 1,6-hexanediol (1,6-HD), an aliphatic alcohol that disrupts weak hydrophobic interactions (Kroschwald *et al.*, 2017). The addition of 1,6-HD reduced MT binding of Spc105-B(1-400) by ~40% when compared with Spc105-B(1-400) in the absence of 1,6-HD (Figure 2D). One possibility for this observation is that both hydrophobic and electrostatic interfaces between Spc105 and the MT contribute to the binding affinity. If this were the case, then there would be an additive inhibitory effect on binding of Spc105-B(1-400) to MTs in the presence of both 500 mM KCl and 1,6-HD. On the contrary, the binding efficiency of the high-salt and 1,6-HD condition (12.5%) was nearly identical to that of the high-salt condition alone (14.6%), suggesting that Spc105 relies predominantly on electrostatic interactions with the MT rather than both charged and hydrophobic interfaces between Spc105 and the MT.

A minimal region of the *Arabidopsis thaliana* protein Cry2 can be employed as an optogenetic tag for inducing protein oligomerization with high spatiotemporal control using 488 nm (blue) light (Bugaj *et al.*, 2013). To examine how oligomerization of the Spc105 NTR affected its behavior in living cells, stable cell lines expressing copper-inducible Spc105-B(1-200) tagged at its C-terminus with mCherry-Cry2 and treated with SiR-tubulin were visualized using spinning-disk confocal microcopy (Figure 2, E and F, and Supplemental Figure S3). Spc105-B(1-200)-mCherry-Cry2 was diffuse throughout the cytoplasm and nucleoplasm and exhibited weak, punctate MT localization in some interphase cells. In mitotic cells, the fluorescence intensity of Spc105-B(1-200)-mCherry-Cry2 was higher in the spindle region than in the surrounding cytoplasm; however, this was not due to specific association with spindle MTs as an identical localization pattern was observed in mitotic cells expressing mCherry-Cry2 (Supplemental Figure S3A), and we have consistently observed similar slight enrichments in the spindle region when overexpressing fluorescent protein tags alone (EGFP, mCherry, etc.) in S2 cells (unpublished observation). The localization pattern of Spc105-B(1-200)-mCherry-Cry2 changed dramatically after exposure to blue light (488 nm) as Spc105 oligomers associated robustly with MTs within seconds of photoactivation in both interphase and mitotic cells (Figure 2, E and F, and Supplemental Videos 5 and 6). Importantly, photoactivated mCherry-Cry2 oligomers did not associate with MTs in interphase or mitotic cells (Supplemental Figure S3A). Interestingly, photoactivated Spc105-B-mCherry-Cry2, which uniformly coated interphase MTs, bound strongly to the spindle poles but was not enriched on MTs in the midspindle (Supplemental Figure S3B). The Cry2 tag has been used to study phase transitions of intrinsi-cally disordered regions (IDRs) in living cells via "optoDroplet" assays (Shin *et al.*, 2017). Somewhat surprisingly, higher expression levels were required to support light-induced oligomerization of Spc105-B(1-200)-mCherry-Cry2 than for the mCherry-Cry2 tag alone (unpublished observation). Thus, fusion of the first 200 amino acids of Spc105 actually lowered the propensity of mCherry-Cry2 to form optoDroplets despite the fact that this is predicted to be an IDR.
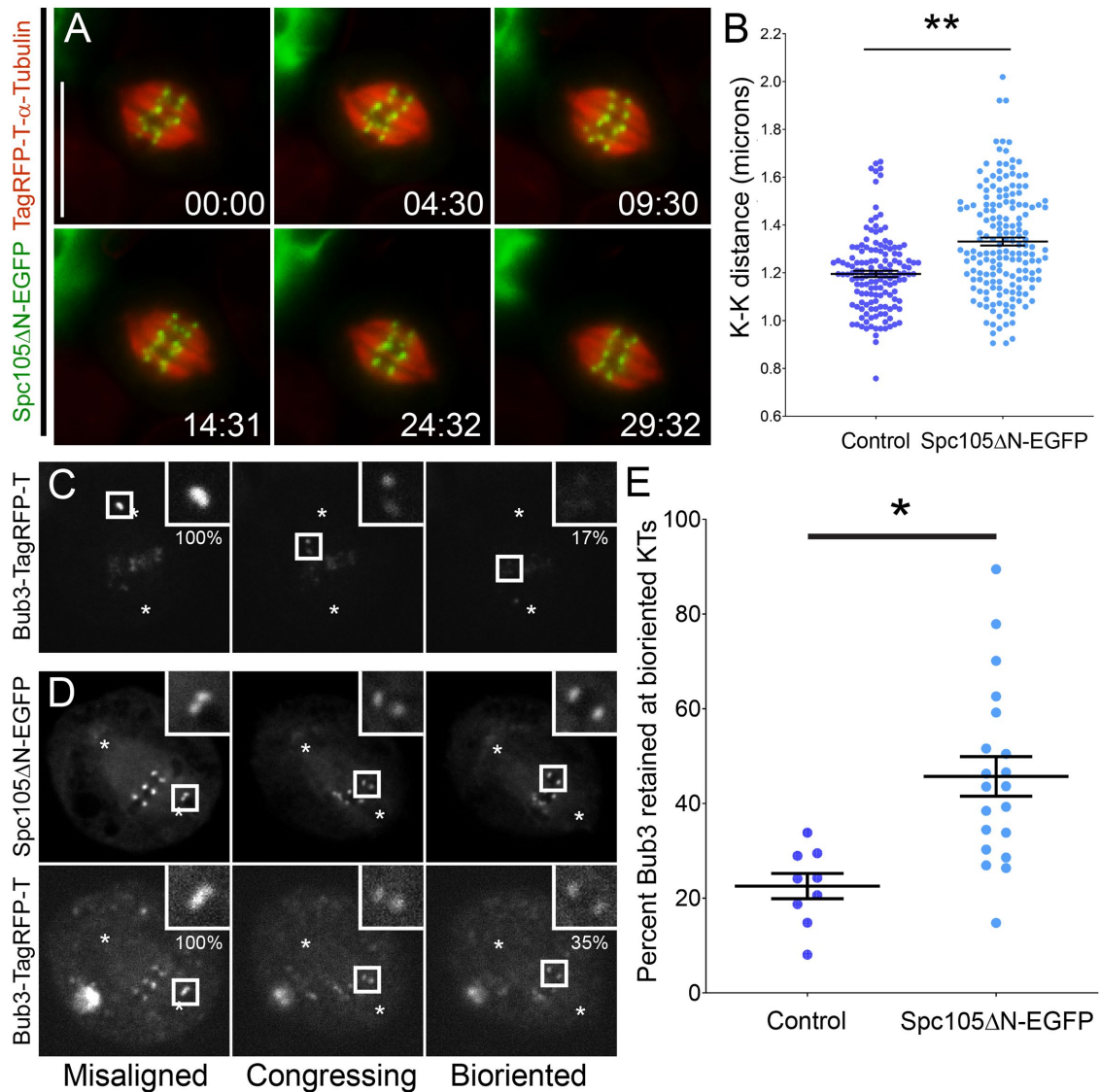
Deletion of the Spc105 NTR results in a metaphase delay with hyperstretched KTs that retain elevated levels of Bub3

We next characterized how the NTR of Spc105 contributes to cell division by expressing a truncated version of Spc105 lacking the first 400 amino acids (Spc105ΔN). While stable cells that expressed full-length Spc105 were readily made, we were unable to make stable cell lines expressing Spc105ΔN due to the mutant exhibiting a dominant negative effect. Thus, all experiments with Spc105ΔN were done via transient transfections in which dividing cells expressing the mutant were found in the population, albeit with decreasing frequency, over the course of ~7–10 d. When Spc105ΔN-EGFP was transfected into cells stably expressing TagRFP-T-α-tubulin, we found that it localized normally, which was expected because the C-terminus of Spc105 targets it to the KT (Venkei *et al.*, 2012). Interestingly, cells expressing the truncation were often delayed in metaphase when compared with cells not expressing Spc105ΔN in the same imaging chamber (Figure 3A and Supplemental Video 7). Furthermore, cells expressing Spc105ΔN exhibited KT hyperstretch as the distance between bioriented KTs (K-K) increased to 1.33 ± 0.02 µm (mean ± SEM) compared with 1.19 ± 0.02 µm in nonexpressing cells (Figure 3B).

The observed metaphase delay in Spc105ΔN-expressing cells led us to next examine the behavior of the checkpoint protein Bub3, which was already shown to bind directly to the central IDR of Spc105 in vitro (Figure 1E). Time-lapse imaging of Bub3-TagRFP-T–expressing cells revealed that Bub3 levels were highest at misaligned KTs and became depleted from KTs during chromosome congression until reaching its nadir (preanaphase onset) at bioriented KTs, which retained ~20% of the Bub3 levels originally at misaligned KTs (Figure 3, C and E, and Supplemental Video 8). Interestingly, bioriented KTs in Spc105ΔN-expressing cells retained twofold higher levels of Bub3 (~46% relative to misaligned KTs) than was measured at bioriented KTs in control cells (Figure 3, D and E). Thus, deletion of the NTR of Spc105 resulted in a metaphase delay with hyperstretched KTs that retained elevated levels of the checkpoint protein Bub3.

Deletion of the Spc105 NTR results in hyperstable KT-MT attachments without mislocalizing active ABK populations

While the KT hyperstretch phenotype observed in Spc105ΔN-expressing cells was indicative of stable (or potentially hyperstable) KT-MT attachments, we next sought to more quantitively assess the nature of attachments by measuring photoactivatable (PA)-GFP-α-tubulin turnover in metaphase spindles. Cells co-transfected with PA-GFP-α-tubulin and either Spc105ΔN (experimental) or full-length Spc105-B (control) were subjected to spinning-disk confocal time-lapse imaging during which 405 nm laser light was focused on a rectangular region adjacent to the metaphase plate to locally photoactivate PA-GFP-α-tubulin molecules in the spindle (Figure 4A and Supplemental Video 9). Broadly speaking, mitotic spindles are made up of more stable KT-MTs and more dynamic non–KT-MTs. The relative abundance and stability ($T_{1/2}$) of each MT population can be measured in a spindle by quantification of its background- and bleach-corrected

FIGURE 3: Deletion of the NTR of Spc105 results in a metaphase delay with elevated levels of Bub3 retained at bioriented KTs. (A) Still frames from wide-field time-lapse imaging of a cell expressing Tag-RFP-T-α-tubulin (red) and Spc105ΔN-EGFP (green) delayed in metaphase. (B) Quantification of the distance between bioriented KTs in metaphase (K-K distance) (control, $n = 144$ KT pairs from 17 cells; Spc105ΔN, $n = 171$ KT pairs from 15 cells). (C) Representative images of still frames from spinning-disk confocal time-lapse imaging of a control cell expressing Bub3-TagRFP-T with insets highlighting Bub3 levels that decline as a misaligned KT pair becomes bioriented. (D) Representative images of still frames from spinning-disk confocal time-lapse imaging of a cell coexpressing Spc105ΔN-EGFP and Bub3-TagRFP-T with insets highlighting the congressing KTs. (E) Quantification of average Bub3 retention at bioriented KTs relative to misaligned KTs in control cells compared with Spc105ΔN-expressing cells (control, $n = 9$ cells; Spc105ΔN, $n = 20$ cells). In C and D, the asterisks denote locations of the spindle poles and the percents below the insets indicate the relative levels of Bub3 at the pair of misaligned and bioriented sister KTs. Displayed times are minutes:seconds. Scale bar is 10 μm. Error bars are SEM. The reported p values were generated by a randomization method: * p value < 0.05, ** p value < 0.005.

PA-GFP signal as it dissipates over time and applying a double-exponential fit to the data (Cimini *et al.*, 2006) (Figure 4B). The flux rate (poleward movement of MT polymer within the spindle) was quantified by measuring the movement of the photoactivated region over time.

PA-GFP-α-tubulin turnover measurements revealed that 75% of the spindle MTs in Spc105ΔN-expressing metaphase cells were KT-MTs compared with only 20% of the spindle MTs in control cells expressing Spc105-B (Figure 4C). Interestingly, consistent with the prior K-K measurements, KT-MTs were more stable in Spc105ΔN-expressing cells as the KT-MT $T_{1/2}$, which is the time for half of the MT polymer to turn over, was 6.6 min compared with 5.1 min in Spc105-B–expressing control cells. The stability of non–KT-MTs was comparable between experimental and control cells as the non–KT-MT $T_{1/2}$ was 32.4 s and 37.6 s for metaphase spindles in Spc105-B– and Spc105ΔN-expressing cells, respectively. Finally, the flux rate was reduced significantly to 0.4 μm/min in cells expressing Spc105ΔN compared with 1.0 μm/min in control cells. Thus, expression of Spc105ΔN resulted in more stable KT-MT attachments within metaphase spindles that exhibited suppressed poleward flux.
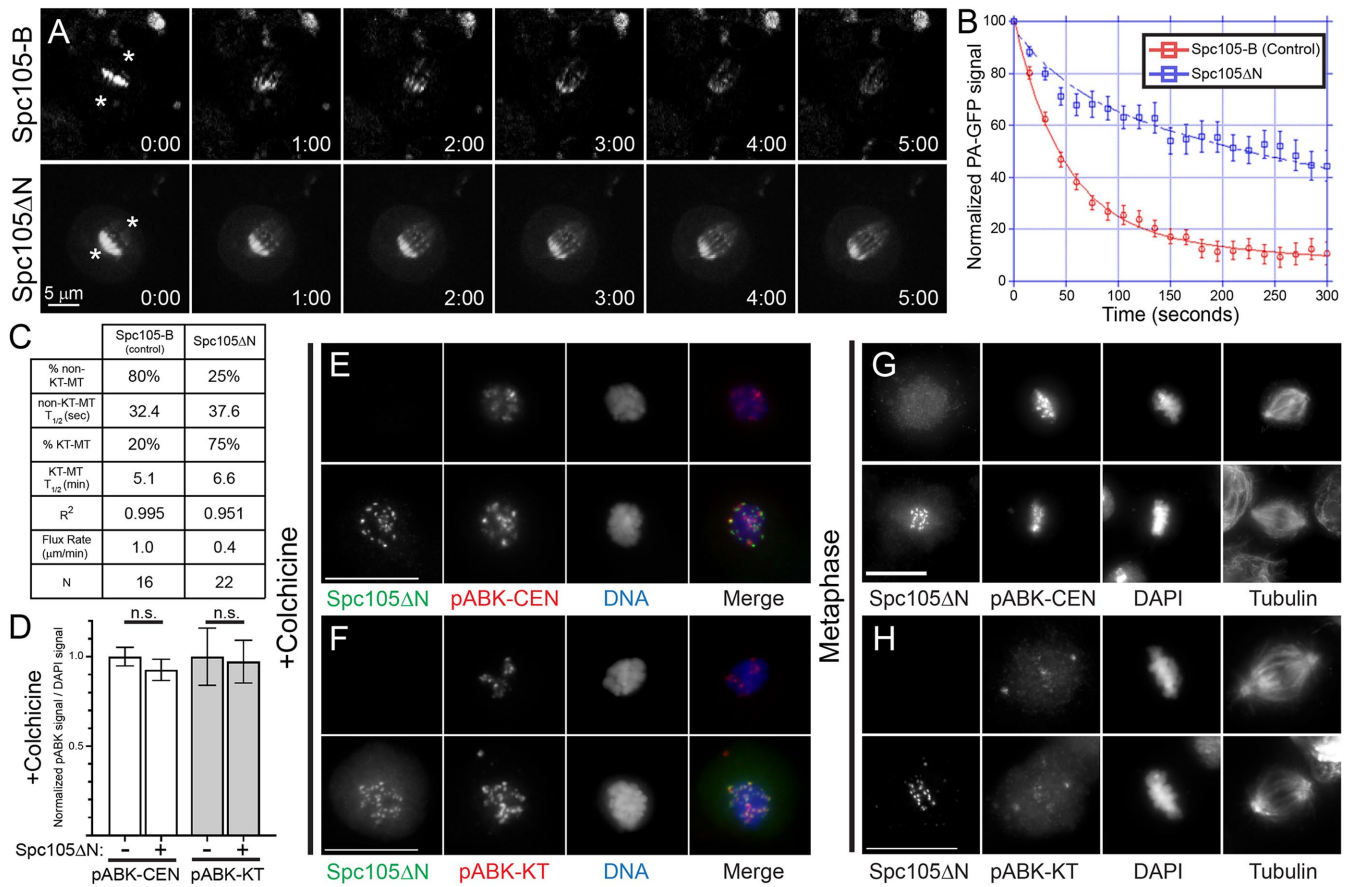
FIGURE 4: Spc105ΔN-expressing cells establish hyperstable KT-MT attachments without affecting ABK activity or localization. (A) Still frames from spinning-disk confocal time-lapse imaging of a metaphase cell coexpressing Spc105-B (top) or Spc105ΔN (bottom) and photoactivatable (PA)-GFP-α-tubulin. (B) Double-exponential fit ($F = A1^{(-k1 \times t)} + A2^{(-k2 \times t)}$) of the decay in PA-GFP signal over time in Spc105-B– and Spc105ΔN-expressing cells (control, $n = 16$ cells; Spc105ΔN, $n = 22$ cells). (C) Summary of the measurements from the double-exponential fits applied in B. (D) Quantification of normalized pABK:DAPI (4',6-diamidino-2-phenylindole) signals in colchicine-treated cells ($n = 30$ cells from three independent experiments for each condition). (E, F) Maximum projections of wide-field fluorescence Z-sections of Spc105ΔN-transfected cells treated with colchicine (25 μM) overnight and stained with anti-GFP (green in merge), anti–pABK-CEN (E, red) or anti–pABK-KT (F, red), and DAPI (blue). (G, H) Representative maximum projections of wide-field fluorescence Z-sections of Spc105ΔN-transfected cells in metaphase stained with anti-GFP (Spc105ΔN), anti–pABK-CEN (G) or anti–pABK-KT (H), DAPI, and anti-tubulin. Nonexpressing and expressing cells from the same coverslips as shown in E–H. Displayed times are minutes:seconds. Scale bars, 5 μm (A, B), 10 μm (E–H). Error bars are SEM. The reported p values were generated by a randomization method: n.s. (not significant) = p value > 0.05.

Prior work reported that the N-terminus of human KNL1 promoted ABK activity and its deletion caused premature stabilization of KT-MT attachments due to reduced phosphorylation of ABK substrates in the outer KT (Caldas et al., 2013). Thus, reduced ABK activity could explain the increased KT-MT attachment stability observed in Spc105ΔN-expressing cells. Multiple populations of active ABK have been identified across the centromere and KT in mammalian cells (DeLuca et al., 2011; Broad et al., 2020). We previously observed distinct populations of active, phosphorylated ABK by immunostaining with two phospho-Aurora kinase antibodies (Ye et al., 2015). Staining with one antibody (referred to here as pABK-CEN) preferentially labeled a population of centromeric phospho-ABK that localized to the inner centromeres at both unattached and bioriented KTs. Another antibody (referred to here as pABK-KT) preferentially labeled a more punctate population of phospho-ABK in close proximity to Ndc80 that was high at unattached KTs and depleted from bioriented KTs. Immunofluorescence for pABK-CEN or pABK-KT was conducted to visualize each of the pools in colchicine-

treated cells transfected with Spc105ΔN. Interestingly, there was not a statistically significant difference between the levels of either the pABK-CEN or pABK-KT populations between Spc105ΔN-expressing and -nonexpressing cells on the same coverslip (Figure 4, D–F). In metaphase, pABK-CEN localized normally to the inner centromeres and pABK-KT was similarly depleted from aligned KTs in Spc105ΔN-expressing and -nonexpressing cells (Figure 4, G and H).

The Spc105 NTR is the primary receptor for PP1-87B at bioriented KTs in *Drosophila* S2 cells

The NTR of Spc105 has two well-conserved PP1-binding motifs (Liu et al., 2010; Rosenberg et al., 2011; Espeut et al., 2012; London et al., 2012; Bajaj et al., 2018) (Figure 2A). Interestingly, depletion of the PP1 orthologue (PP1-87B) from S2 cells yielded the same phenotype as was observed in Spc105ΔN-expressing cells—a metaphase delay with stable KT-MT attachments (Moura et al., 2017). Thus, we characterized PP1-87B in living cells and investigated whether deletion of the Spc105 NTR impacted PP1-87B localization
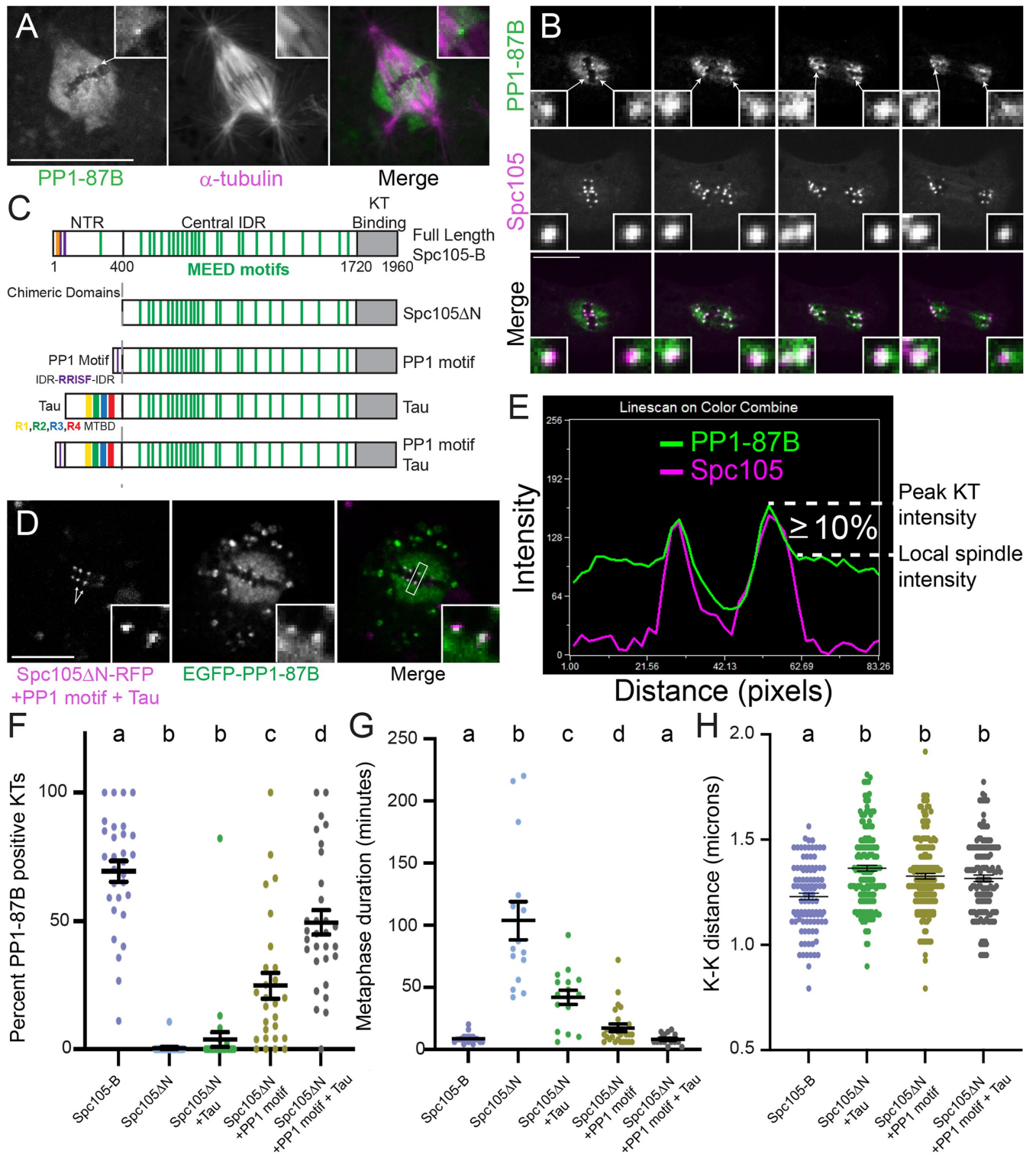
FIGURE 5: Dissecting the relative contributions of PP1-87B recruitment and MT binding by Spc105 to SAC satisfaction. (A) Maximum projections of spinning-disk confocal Z-sections of a metaphase cell coexpressing RFP-PP1-87B (green) and EGFP-α-tubulin (magenta). Arrow points to the puncta of PP1-87B shown in the zoomed inset. (B) Still frames from a spinning-disk confocal time lapse of a cell coexpressing RFP-PP1-87B (green) and Spc105-EGFP (magenta) progressing from metaphase through anaphase. Arrows point to the KTs shown in the zoomed insets. (C) Schematics of full-length Spc105-B, Spc105ΔN, and the Spc105ΔN chimeras. (D) Spc105ΔN-TagRFP-T + PP1 motif + Tau (magenta) colocalizes with EGFP-PP1-87B (green) in a representative spinning-disk confocal plane. Arrows point to the KTs shown in the zoomed insets. Boxed region highlights the KT pair subjected to linescan analysis shown in E. (E) Representative linescan on the merged image shown in D highlighting how PP1-87B–positive KTs were identified. (F) Percent of PP1-87B–positive KTs in cells coexpressing fluorescently tagged PP1-87B and Spc105-B, Spc105ΔN, or the indicated Spc105ΔN chimera (Spc105-B, n = 30 cells; Spc105ΔN, n = 28 cells; Spc105ΔN + Tau, n = 29 cells; Spc105ΔN + PP1

to KTs. Stable S2 cells coexpressing RFP-PP1-87B and EGFP-α-tubulin were generated to visualize the localization of PP1 throughout mitosis in living cells, which has been quite limited to date (Liu *et al.*, 2010). PP1-87B enveloped the body of the mitotic spindle throughout mitosis in a manner reminiscent of spindle matrix components (Walker *et al.*, 2000; Qi *et al.*, 2004, 2005; Rath *et al.*, 2004; Lince-Faria *et al.*, 2009) without apparent enrichment on spindle MTs but with discrete puncta at the end of KT-fibers in metaphase (Figure 5A and Supplemental Video 10). It was confirmed that the observed puncta were localized to KTs as EGFP-PP1-87B colocalized with Spc105-TagRFP-T from metaphase through anaphase (Figure 5B and Supplemental Video 11). We next cotransfected PP1-87B and either full-length Spc105-B or Spc105ΔN to characterize how PP1 localization was affected by deletion of the NTR (Figure 5C). A linescan-based method was used to quantify PP1-87B localization to KTs in the context of the high local spindle matrix–like signal. In brief, linescans were drawn through bioriented KT pairs and if a PP1-87B peak 1) overlapped with a Spc105 peak and 2) was at least 10% higher than the local spindle PP1-87B signal, then the KT was scored as PP1-87B positive (Figure 5, D and E). Using this method, 69.4 ± 4.1% (mean ± SEM) of KTs in Spc105-B–expressing cells scored as PP1 positive versus only 0.4 ± 0.4% in Spc105ΔN-expressing cells (Figure 5F).

The N-terminal activities of Spc105 contribute to SAC satisfaction

We next sought to understand the molecular mechanisms by which the Spc105 NTR contributed to timely SAC satisfaction. The Spc105ΔN truncation removed both PP1-87B– and MT-binding activities. To dissect the relative contributions of each of these activities to Spc105's function in SAC satisfaction, Spc105 chimeras were created that restored each activity individually and in combination (Figure 5C). We conducted live-cell imaging of cells expressing Spc105-B, Spc105ΔN, or one of the chimeras to quantify metaphase duration (Figure 5G) and measured the efficiency of PP1-87B recruitment to bioriented KTs by coexpressing fluorescently tagged PP1-87B with each of the chimeras (Figure 5F). Metaphase duration, which was defined as the time between biorientation of the last pair of sister KTs and anaphase onset, was 8.7 ± 0.8 min (mean ± SEM) in control cells expressing full-length Spc105-B. By contrast, Spc105ΔN-expressing cells were delayed in metaphase for 104 ± 15 min. Replacing the NTR of Spc105 with the intrinsically disordered MT-associated protein dTau (*Drosophila* Tau) resulted in a reduction in the metaphase delay to 42 ± 6 min, yet the percent of PP1-87B–positive KTs (3.8 ± 2.8%) was not statistically significantly different from that measured in Spc105ΔN-expressing cells (0.4 ± 0.4%) (Figure 5, F and G). Thus, MT binding contributed to the timing of SAC satisfaction independent of recruiting detectable levels of PP1-87B above the levels observed for Spc105ΔN.

To test the contribution of PP1-87B recruitment to SAC satisfaction, a second chimera was generated in which the PP1-binding motif (RRISF) flanked by intrinsically disordered regions (IDRs) was introduced at the N-terminus of Spc105ΔN (Figure 5C). Addition of the PP1 motif resulted in a statistically significant increase in the percentage of PP1-87B–positive KTs (24.8 ± 5.1%) relative to cells expressing either the Spc105ΔN or the Tau-Spc105ΔN chimera (Figure 5F). Metaphase duration in cells expressing the PP1 chimera was 17.2 ± 3.0 min, a rescue that was considerably stronger than that of Tau-Spc105ΔN, but not a complete rescue as metaphase was still statistically significantly longer (~2×) than in control cells (Figure 5G). A third chimera introducing both the PP1- and MT-binding activities into Spc105ΔN was generated that included the RRISF site followed by dTau (Figure 5C). Interestingly, the combination of the PP1 motif and Tau resulted in higher levels of PP1 recruitment to KTs (49.5 ± 4.8%) than the PP1 motif alone, but statistically significantly lower than the 69.4 ± 4.1% measured in Spc105-B–expressing control cells (Figure 5F). Nonetheless, expression of the PP1 motif + Tau-Spc105ΔN chimera produced a complete rescue of the metaphase delay phenotype with a metaphase duration of 8.2 ± 0.8 min—statistically indistinguishable from the 8.7 ± 0.8 min measured in control cells (Figure 5G). This was not a consequence of a SAC defect as cells expressing the PP1 motif + Tau-Spc105ΔN chimera mounted a mitotic arrest response to overnight treatment with colchicine (7.8 ± 0.8-fold increase in the mitotic index relative to dimethyl sulfoxide (DMSO)–treated cells; *n* = 2 overnight treatments) that was comparable to that of cells that were not expressing the chimera (6.7 ± 1.1-fold increase; *n* = 2 overnight treatments). Interestingly, each of the chimeras exhibited increased K-K distances in metaphase compared with the Spc105-B–expressing control cells (Figure 5H). Thus, the chimeras may not rescue the hyperstable KT-MT attachment phenotype despite the fact that they reduced metaphase duration relative to the Spc105ΔN mutant. Taken together, data from the chimeras support the conclusion that PP1 recruitment and, to a lesser extent, MT binding by the Spc105 NTR make separable contributions to SAC satisfaction in *Drosophila* S2 cells.

The MT- and PP1-binding activities of Spc105 are not mutually exclusive in *Drosophila* S2 cells

Human KNL1 interacts with PP1 and MTs in a mutually exclusive manner in vitro (Bajaj *et al.*, 2018)—a finding that, if applicable to *D. melanogaster* Spc105 in vivo, is difficult to reconcile with our conclusion that the MT- and PP1-binding activities both contribute to SAC satisfaction at bioriented KTs. To further probe the binding of Spc105 to PP1 and MTs in cells, the Cry2-based optogenetic assay previously employed to characterize MT binding (Figure 2, E and F) was applied to cells coexpressing copper-inducible Spc105-B(1-200)-mCherry-Cry2 and EGFP-PP1-87B under the control of a promoter driving constitutive low-level expression. If binding of Spc105 to MTs and PP1 was mutually exclusive in cells, then PP1-87B would associate

motif, *n* = 27 cells; Spc105ΔN + PP1 motif + Tau, *n* = 30 cells). (G) Metaphase durations (defined as the time between biorientation of last sister KT pair and anaphase onset) in cells expressing Spc105-B, Spc105ΔN, or the indicated Spc105ΔN chimera (Spc105-B, *n* = 20 cells; Spc105ΔN, *n* = 15 cells; Spc105ΔN + Tau, *n* = 16 cells; Spc105ΔN + PP1 motif, *n* = 26 cells; Spc105ΔN + PP1 motif + Tau, *n* = 20 cells). (H) Quantification of the K-K distance between bioriented KTs in metaphase (Spc105-B, *n* = 104 KT pairs from 13 cells; Spc105ΔN + Tau, *n* = 181 KT pairs from 19 cells; Spc105ΔN + PP1 motif, *n* = 181 KT pairs from 29 cells; Spc105ΔN + PP1 motif + Tau, *n* = 138 KT pairs from 19 cells). Each dot in the scatter plots for F and G represents measurements from an individual cell. An average of 24 KTs per cell were analyzed for the data presented in F. Scale bars, 10 μm. Error bars are SEM. The different letters above each scatter plot column indicate significant differences (*p* < 0.05) determined by a randomization test with all pairwise combinations. Same letters indicate that the difference is not significant (*p* > 0.05).
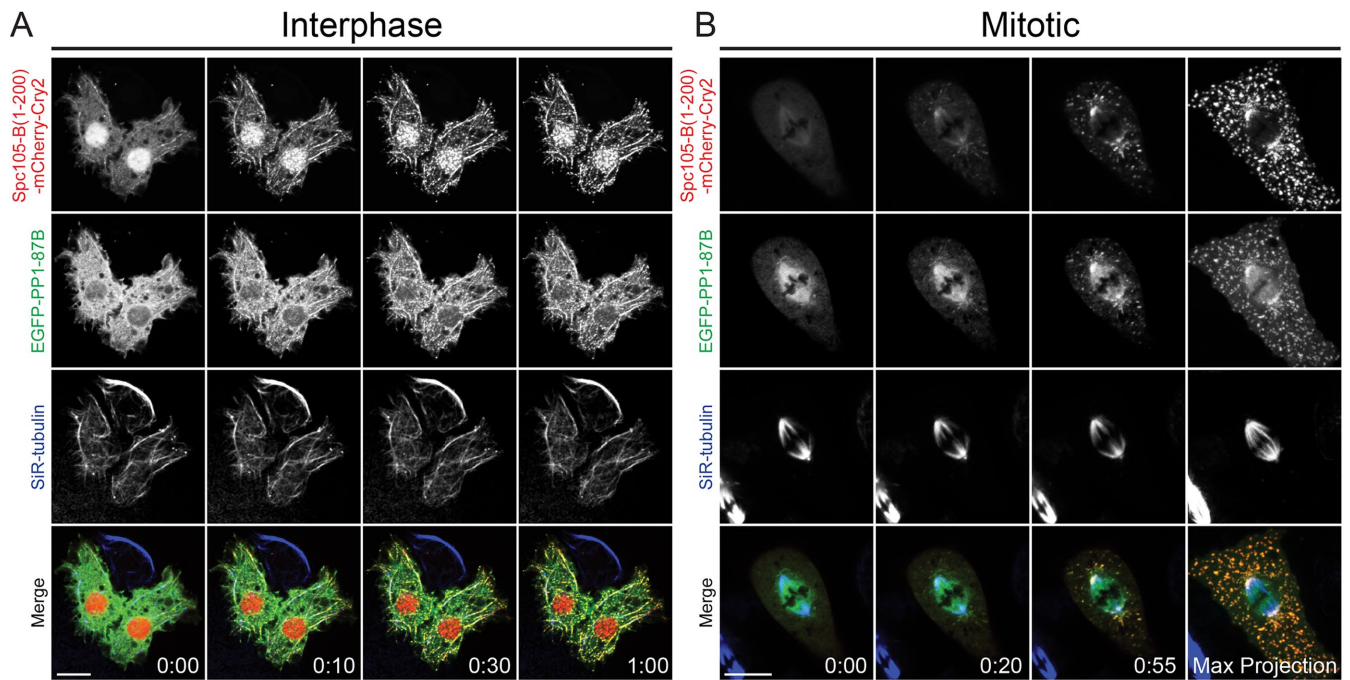
FIGURE 6: Optogenetic oligomerization of the NTR of Spc105 supports its binding to MTs and PP1-87B simultaneously. (A, B) Representative still frames from spinning-disk confocal time-lapse imaging of interphase (A) or mitotic (B) cells coexpressing Spc105-B(1-200)-mCherry-Cry2 (red) and EGFP-PP1-87B (green) with the MTs labeled in far-red with SiR-tubulin (blue). A maximum projection of confocal Z-sections acquired ~1 min after the initial photo-oligomerization of the mitotic cell is shown in B to highlight colocalization of the PP1-87B with both spindle-associated and cytoplasmic oligomers of Spc105-B(1-200). The cells were subjected to continued rounds of photo-oligomerization via 200 ms pulses/exposures with the 488 nm laser to visualize EGFP-PP1-87B localization. The first 488 nm pulse was applied at 00:00 following acquisition of the mCherry channel to visualize Spc105-B(1-200)-mCherry-Cry2 localization before photo-oligomerization. Displayed times are minutes:seconds. Scale bars, 10 μm.

with cytoplasmic oligomers but not with MT-bound Spc105-B(1-200). To the contrary, PP1-87B was rapidly recruited to MTs upon photo-oligomerization of Spc105-B(1-200)—exhibiting uniform colocalization with Spc105 on MTs in interphase cells (Figure 6A and Supplemental Video 12) and becoming enriched with Spc105 near spindle poles and on astral MTs in mitotic cells (Figure 6B and Supplemental Video 13). PP1-87B also colocalized with non–MT-bound cytoplasmic oligomers of Spc105-B(1-200) in interphase and mitosis. The observed colocalization was specific to PP1-87B and Spc105-B(1-200) as there was no colocalization observed in photoactivated cells coexpressing either EGFP and Spc105-B(1-200)-mCherry-Cry2 (Supplemental Figure S4A) or EGFP-PP1-87B and mCherry-Cry2 (Supplemental Figure S4B). Thus, application of the optogenetic oligomerization method to the NTR provided convincing evidence that Spc105 oligomers simultaneously bind MTs and PP1 under physiological conditions in *Drosophila* S2 cells.

DISCUSSION

The phosphoregulatory circuit in *Drosophila melanogaster*

Phosphorylation of repeated motifs in KNL1 orthologues is the key mediator of checkpoint protein recruitment to KTs in every model system that has been examined, with the exception of flies. This work clarifies the picture in *D. melanogaster* by demonstrating that a phosphoregulatory circuit exists that relies on ABK activity (rather than Mps1 or PLK1) promoting the interaction between Spc105 and Bub3. We cannot exclude the possibility that Aurora A kinase (AAK), which targets KT substrates (DeLuca *et al.*, 2018) especially near spindle poles (Chmátal *et al.*, 2015; Ye *et al.*, 2015), may also contribute to this mechanism. The fact that Bub3 binds to unphosphor-

ylated 10xMEED in vitro suggests that lower-affinity interactions between the two proteins may exist in the absence of phosphorylation, potentially due to electrostatic interactions between the phosphomimetic MEED motifs in Spc105 and Bub3. AAK activity and/or direct electrostatic interactions, independent of phosphorylation, may account for the residual levels of Bub3 observed at unattached KTs in cells following ABK inhibition. Further investigation of this phenomenon and the nature of the Bub3-Spc105 interface and how it is regulated is warranted. Although Mps1 is not directly involved in the regulation of Bub3 binding to KTs in *Drosophila* S2 cells (Conde *et al.*, 2013), our findings demonstrate that the utilization of a phosphoregulatory circuit (here controlled by ABK) is evolutionarily conserved in flies.

Current models hold that recruitment of PP1 to the NTR of KNL1 homologues contributes to SAC satisfaction by promoting dephosphorylation of the MELT motifs and, consequently, reducing their affinity for the Bubs. Similar phosphoregulatory mechanisms likely promote SAC satisfaction in flies because it is well established that PP1 opposes ABK activity. Interestingly, a prior study in *D. melanogaster* reported that BubR1 recruitment to KTs and checkpoint function were unaffected in embryos expressing Spc105 lacking a portion of the central IDR, leading the authors to conclude that the middle of Spc105 was dispensable (Schittenhelm *et al.*, 2009). Yet our findings support the conclusion that the Spc105 IDR is an important platform for SAC signaling in *D. melanogaster*. One possible explanation for this discrepancy is that the mutant used in the prior study possessed more than a single MEED motif (as presumed at that time) because subsequent analyses identified at least six more repeats in *D. melanogaster* Spc105

(Vleugel *et al.*, 2013; Tromer *et al.*, 2015) including motifs that would have been retained in the prior Spc105 deletion mutants (Schittenhelm *et al.*, 2009). Importantly, the presence of just one additional motif may have been sufficient to support SAC signaling given that as few as two to three MELT motifs support the SAC-regulating functions of human KNL1 (Zhang *et al.*, 2014).

Implications for MT binding by Spc105 orthologues

In this study we demonstrated that Spc105 binds MTs. Our results support the interpretation that affinity for the MT is mediated by electrostatic interactions with basic patches in Spc105 and that higher avidity is accomplished through homo-oligomerization—most likely via hydrophobic interactions. Interestingly, a hydrophobic region in the first ~240 amino acids of *C. elegans* KNL-1 has been shown to mediate oligomerization in vitro (Kern *et al.*, 2015). While the data suggest that the basic patch at the immediate N-terminus (present in the Spc105-B variant) is the highest-affinity interaction site, additional lower-affinity patches must exist in the NTR because Spc105-A(1-400) still bound to MTs albeit with lower efficiency. Indeed, recent work has identified other basic regions beyond the immediate N-terminus that contribute to MT binding in human KNL1 and budding yeast Spc105 (Bajaj *et al.*, 2018; Roy *et al.*, 2019). The preferential binding of oligomerized Spc105-B(1-200)-mCherry-Cry2 to spindle poles and astral MTs suggests that MT binding by Spc105 is spatially regulated in mitosis. Interestingly, ABK and AAK may differentially inhibit MT binding because oligomerized Spc105 localization was lowest in the midspindle where ABK activity is highest and abundant at spindle poles and astral MTs where AAK activity is highest (Ye *et al.*, 2015). The observation of rapid MT binding by Spc105-B(1-200)-mCherry-Cry2 following photoactivation also revealed the importance of avidity to the functional affinity of Spc105 for MTs and, therefore, its function in SAC satisfaction. Interestingly, deletion of the hydrophobic oligomerization region in *C. elegans* KNL-1 phenocopied mutations in the basic MT-binding patch at the immediate N-terminus as both mutant worms exhibited reproducible delays in anaphase onset (Espeut *et al.*, 2012; Kern *et al.*, 2015). As in other aspects of KT biology, this mechanism suggests that multiple and parallel low-affinity interactions additively contribute to functionality in vivo.

The MT- and PP1-binding activities in Spc105 regulate SAC signaling but are dispensable for establishing stable KT-MT attachments

The NTR of Spc105 binds directly to MTs in vitro, but this activity is not required for establishing stable end-on KT-MT attachments in cells. In fact, deletion of the NTR resulted in KT-MT attachment hyperstability without evidently impacting active ABK localization, which is distinct from the effects of deleting the N-terminus of human KNL1 (Caldas *et al.*, 2013). It is possible that ABK is differentially regulated vis-à-vis the Spc105 NTR in *Drosophila*; alternatively it may be due to the fact that we deleted a (relatively) smaller portion of the N-terminus of Spc105 (containing only 1 out of ~25 MEED motifs) than was deleted in the N-terminal truncations of human KNL1 that impacted ABK activity (Caldas *et al.*, 2013). Regardless, the K-K hyperstretch and KT-MT hyperstability phenotypes in cells expressing Spc105ΔN do not appear to be a result of significant mislocalization of active ABK from the inner centromere or KT—a conclusion that is consistent with retention of Bub3 at bioriented KTs in Spc105ΔN-expressing cells because Bub3's recruitment depends on ABK activity in S2 cells. Thus, it is currently unclear why the Spc105ΔN mutant exhibits KT-MT attachment hyperstabil-

ity. The increased K-K distances observed in cells expressing the Spc105 chimeras suggests that the regulatory mechanism depends on the NTR but that PP1 recruitment and MT binding are insufficient to rescue the hyperstability phenotype.

What, therefore, is the biological role of the MT interactions mediated by Spc105? Our data are consistent with the interpretation that MT binding by the NTR acts as a SAC sensor (Espeut *et al.*, 2012) rather than in making load-bearing KT-MT attachments (Caldas *et al.*, 2013; Zhang *et al.*, 2014). It is also noteworthy that the phenotype observed in Spc105ΔN-expressing cells (hyperstretched, hyperstable KT-MT attachments with reduced spindle flux) is similar to that observed in mammalian PtK1 cells following microinjection of an antibody that binds near the CH domain of the Ndc80 complex component HEC1 (DeLuca *et al.*, 2006). It will, therefore, be important to investigate whether there is cross-talk between the NTR of Spc105 and the Ndc80 complex given the latter's role as the key mediator of stable end-on attachments. The KNL1-bound pool of PP1 has also been implicated in promoting KT-MT attachment stability (Liu *et al.*, 2010; Meadows *et al.*, 2011). The facts that 1) Spc105ΔN-expressing cells fail to satisfy the SAC with normal kinetics yet 2) establish hyperstable KT-MT attachments that 3) fail to recruit PP1-87B altogether support the conclusion that the Spc105-bound pool of PP1-87B primarily promotes SAC satisfaction but not KT-MT attachment stability in *Drosophila* S2 cells. This conclusion aligns well with findings from a recent study of budding yeast Spc105 (Roy *et al.*, 2019).

PP1 recruitment by Spc105 and possible synergy between the MT- and PP1-binding activities

The Spc105 chimera studies provided useful insights into the physiologically and functionally relevant aspects of PP1 recruitment and MT binding by KNL1 in vivo. Multiple studies have identified the second motif (RVXF) as the key binding site for PP1 (Liu *et al.*, 2010; Rosenberg *et al.*, 2011; Espeut *et al.*, 2012; Bajaj *et al.*, 2018), but the SILK and RVXF motifs have also been shown to work cooperatively to mediate the highest-affinity interaction between PP1 and KNL1 as well as other PP1 substrates (Hendrickx *et al.*, 2009; Meadows *et al.*, 2011; Bajaj *et al.*, 2018). The fact that the RRISF-Spc105ΔN chimera recruited less PP1-87B than full-length Spc105-B supports the conclusion that both the SILK and RVXF motifs are required for maximal PP1 recruitment in vivo, consistent with in vitro data (Meadows *et al.*, 2011; Bajaj *et al.*, 2018). Functionally, however, SAC satisfaction was significantly accelerated in the RRISF chimera and fully rescued in the RRISF + Tau chimera, each of which had less than maximal PP1 recruitment to KTs. Thus, a critical threshold of Spc105-bound PP1 that is sufficient to satisfy the SAC can be recruited in the absence of the SILK motif and, therefore, without the highest possible binding affinity between Spc105 and PP1-87B. It remains to be established the situations in vivo in which the SILK motif becomes functionally important for PP1 binding to KTs with regard to SAC satisfaction.

It was particularly interesting that the RRISF + Tau chimera more effectively recruited PP1-87B than the RRISF chimera despite the fact that the Tau chimera did not recruit PP1-87B (Figure 5, F and G). What could explain the synergy between MT binding and PP1 recruitment to Spc105? The spatial positioning model offers one possibility (Liu *et al.*, 2008, 2010; Maresca and Salmon, 2010), namely that MT binding by Tau in the chimeric protein could position the RRISF motif, which cannot effectively bind PP1 when it is phosphorylated (Liu *et al.*, 2010; Bajaj *et al.*, 2018; Roy *et al.*, 2019), farther away from a source of ABK activity at the centromere or KT to favor PP1 recruitment. In support of this hypothesis,

recent work in human cell lines concluded that stretching the outer KT away from the inner KT promoted PP1 recruitment to bioriented KTs (Uchida *et al.*, 2021). Mutually exclusive binding of Spc105 to MTs and PP1 (Bajaj *et al.*, 2018) would be inconsistent with a synergistic model; however, Spc105-B(1-200)-mCherry-Cry2 oligomers bound to both MTs and PP1-87B under physiological conditions in living cells. Because light-induced Spc105 clusters recapitulate the multivalent nature of the KT environment, which contains >100 Spc105 molecules (Schittenhelm *et al.*, 2010; Lawrimore *et al.*, 2011; Suzuki *et al.*, 2015), it is reasonable to conclude that Spc105 oligomers would also bind MTs and recruit PP1 in the context of bioriented KTs. Clearly, further investigation of the interplay between MT binding and PP1 recruitment by Spc105 in living cells is necessary.

MT binding by Spc105 as a direct and separable input to SAC satisfaction

Our data are consistent with MT binding contributing to SAC satisfaction through a synergistic mechanism via promotion of PP1 recruitment, but they also support the non–mutually exclusive conclusion that MT binding by Spc105 makes a direct contribution to silencing the SAC. How could MT binding be translated into SAC satisfaction independent of PP1 recruitment? It is compelling to envision a mechanical mechanism in which MT binding introduces tension-dependent structural changes in the intrinsically disordered Spc105 that contribute to extinguishing the SAC (Audett and Maresca, 2020; Broad *et al.*, 2020; Uchida *et al.*, 2021). Interestingly, a recent study in which in-depth, image-based analyses of protein ensembles were applied to the human KT led the authors to propose that KNL1 may act as a tension sensor by "unraveling" to relay tension (Roscioli *et al.*, 2020). The possibility that KNL1 regulates the SAC through tension sensing via conformational deformation of its IDRs is an exciting hypothesis worth testing.

MATERIALS AND METHODS
Protein purification
All protein expression constructs were transformed via heat shock into Rosetta (DE3) *Escherichia coli*. After reaching an OD_{600} of ~0.5, expression was induced by adding 0.25 mM isopropyl β-D-1-thiogalactopyranoside (IPTG) and incubating for 12–16 h at 16°C. Cultures were pelleted in a Sorvall RC-5 centrifuge in a GSA rotor at $5000 \times g$ for 30 min at 4°C, and pellets were resuspended in HEPES purification buffer unless otherwise indicated (50 mM HEPES, pH 7.4, 100 mM KCl, 1 mM $MgCl_2$, 1 mM dithiothreitol [DTT], 10% glycerin, and Roche protease inhibitor cocktail). Cells were lysed using an EmulsiFlex-B30 cell disruptor (Avestin) and spun at 15,000 × g for 30 min at 4°C in a Sorvall centrifuge in an SS-34 rotor. The lysate was incubated on either amylose or nickel resins or magnetic Strep-Tactin–coated MagStrep "type 3" XT magnetic beads, depending on the affinity tags and purification needs for 1 h at 4°C. The lysate–bead mixture was poured over a column or retrieved on a magnet, washed with HEPES purification buffer (His and MBP purifications) or Strep-Tactin XT (TST purifications) wash buffer (IBA Lifesciences) and then eluted with 400 mM imidazole for His-tag purifications, 250 mM -maltose for MBP-tag purifications, or Strep-Tactin XT elution buffer (IBA Lifesciences) according to the manufacturer's protocol for TST purifications. Eluted proteins were dialyzed into HEPES purification buffer overnight in a 10 kDa MWCO dialysis cassette and an additional 2 h in fresh buffer the following morning. The protein was then removed from the dialysis cassette and spun down for 10 min at 15,000 rpm in an Eppendorf tabletop microcentrifuge (model 5424) at 4°C. The concentration was determined

using a Bradford assay (BioRad), followed by aliquoting and flash freezing before being stored at –80°C. The Spc105(1-400) variants (A and B) were purified in a Tris purification buffer (10 mM Tris, pH 8, 150 mM KCl, 1 mM $MgCl_2$, 1 mM DTT, and 0.1% Triton) supplemented with 0.5 M -arginine monohydrochloride (Sigma-Aldrich).

In vitro kinase assays
The in vitro kinase assay was performed using the Sli15(INBOX)-Ipl1-6His (construct courtesy of the Biggins lab), which was purified using the methods outlined above with the HEPES purification buffer. The Sli15(INBOX)-Ipl1-6His was preactivated by incubating with 0.2 mM ATP-MgCl$_2$ (pH 7.0) and 1× phosphatase inhibitor cocktail (PhoSTOP-Roche) for 20 min at 30°C. The activated Sli15(INBOX)-Ipl1-6His was then incubated with MBP-Spc105(10xMEED)-TST in HEPES kinase buffer (20 mM HEPES, pH 7.4, 100 mM KCl, 10 mM $MgCl_2$, 1 mM DTT) + 1× PhoSTOP Roche for 20 min at 30°C.

For phosphatase treatment, the Ipl1 + Spc105 kinase mixture was bound to washed magnetic Strep-Tactin-XT beads for 30 min at room temperature. The beads were next resuspended in 1× FastAP buffer (Thermo Fisher Scientific) with or without 10 U of FastAP enzyme (Thermo Fisher Scientific) and incubated for 1 h at 37°C. After the beads were washed three times with 1× FastAP buffer, the mixture was eluted into 1× SDS and run on a 10% SDS–PAGE gel. The proteins were detected via Western blotting and/or Coomassie staining.

Spc105 pull downs with Bub3-EGFP
Sli15(INBOX)-Ipl1-6His was activated as previously described. Magnetic Strep-Tactin-XT beads were preblocked with 10 mg/ml bovine serum albumin (BSA) in HEPES kinase buffer for 1 h. To cleave off the MBP tag, MBP-Bub3-EGFP was dialyzed in the Slide-A-Lyzer MINI Dialysis 10 kDa MWCO device (Thermo Fisher Scientific) 2 × 15 min into Factor Xa buffer (20 mM Tris-HCl, pH 8, 100 mM NaCl, and 2 mM $CaCl_2$) and incubated with Factor Xa Protease (New England Biolabs) for 3 h at room temperature. Factor Xa inhibitor (CALBiochem 251700) was then added at a final concentration of 2 µM and the cleaved Bub3-EGFP was then dialyzed 2 × 15 min in 250 ml of fresh HEPES kinase buffer. Pull-down mixtures of 0.15 µM MBP-Spc105(10XMEED)-TST or MBP-TST and 1.5 µM Bub3-EGFP (10-fold molar excess) were incubated in HEPES kinase buffer with 1 mg/ml BSA and 1xPhoSTOP for 1 h at 30°C in the presence or absence of activated Sli15(INBOX)-Ipl1-6His. After the incubation period, the BSA preblock was removed from the Strep-Tactin-XT magnetic beads, and the beads were washed 3 × 100 µl on a MagRack 6 (General Electric) with HEPES kinase buffer. After removal of the final wash, the pull-down mixtures were added to the washed beads, vortexed, and incubated at room temperature for 30 min with flicking every 5 min to maintain the beads in suspension. The beads were then recovered on the magnet, washed 3 × 100 µl in the HEPES kinase buffer, and eluted in 1× SDS sample buffer after removal of the final wash. The beads were incubated in the SDS sample buffer for 5 min before retrieving them on the magnet and removing the elution sample, which was then boiled at 98°C for 5 min before running on a 10% SDS–PAGE gel and subjecting the samples to Western blot analyses. Band intensities from three independent pull-down experiments were quantified using ImageJ.

In vitro microtubule TIRF assay
Taxol-stabilized MTs were made by supplementing 10 µl of 100 µM unlabeled tubulin with 1% Dylite-649–labeled tubulin (Cytoskeleton) with an equal volume of MT polymerization buffer (1xBRB80, 5 mM $MgCl_2$, 2 mM GTP, 66.6% glycerol). MTs were polymerized at

37°C for 30 min. Taxol was added at 5 µM final concentration, and the mixture was incubated for 5 min at 37°C. Taxol was then added up to a final concentration of 20 µM and the mixture was incubated for an additional 5 min at 37°C. The polymerized Taxol-stabilized MTs were spun down at room temperature in an Eppendorf benchtop microcentrifuge at 15,000 rpm for 20 min to pellet MTs, which were then resuspended in 20 µl of 1xBRB80 + 20 µM Taxol. Taxol-stabilized MTs were used for experiments within 3 d of being made.

In some instances, to reduce the amount of degradation products in the Spc105-B variant preparations used in the MT-binding assays, His purifications (described above) were subjected to sequential TST purifications in which the flow through from an initial incubation with Strep-Tactin-XT magnetic beads was rebound to fresh beads and eluted. The purified Spc105 variants (Spc105-B(1-400) and Spc105-A(1-400)) were then diluted into the Tris purification buffer (described above) containing 0.1 M -arginine monohydrochloride and precleared in a TLA-100 rotor in a Beckman Coulter Optima Max-TL ultracentrifuge for 20 min at 80,000 rpm at 4°C before being used in the MT-binding assays.

Flow chambers were made by adhering an acid-washed and silanized glass coverslip to a glass slide using double-sided tape, leaving a chamber volume of ~10 µl. Anti-tubulin antibody YL1/2 (Abcam) was diluted to 100 µg/ml in 1xBRB80 and incubated in the chamber for 5 min. Five percent Cellomics Pluronic F127 blocking solution (Thermo Scientific) was diluted into 1xBRB80 and then incubated in the chamber for 5 min by wicking the solution through the chamber using Whatman paper (Whatman Limited). Taxol-stabilized 647-labeled microtubules (1 µM) were then flowed into the chamber via wicking and incubated for 5 min before washing, via wicking, 2 × 10 µl with 1xBRB80 + 20 µM Taxol. Precleared ultracentrifuged Spc105 variants were diluted to 50 nM in Tris purification buffer with 100 mM -arginine monohydrochloride, 20 µM Taxol, and 1 mg/ml BSA. The high-salt chambers had Tris purification buffer with 500 mM KCl, and the 1,6-hexanediol chambers contained 5% 1,6-HD (Sigma Aldrich) in Tris buffer. Sli15(INBOX)-Ipl1-6His was preactivated and incubated in the same conditions as previously described, with the exception of using Tris buffer instead of HEPES kinase buffer.

Chambers were imaged on a TIRF–spinning-disk system assembled on an Eclipse Ti-E inverted microscope (Nikon) equipped with a Borealis (Andor) retrofitted CSU-10 (Yokogawa) spinning-disk head and two ORCA-Flash4.0 LT Digital CMOS camera (Hamamatsu) using a 100 × 1.49 numerical aperture (NA) Apo differential interference contrast TIRF objective (Nikon). Metamorph software (Molecular Devices) was used to control the imaging system. Imaging began approximately 2 min after adding the Spc105 at 1 × 1 camera binning and 100 ms TIRF-488, and 50 ms TIRF-641 exposures. Each chamber was imaged for no more than 20 min after the Spc105 was introduced.

Quantification of MT binding was done in ImageJ by first measuring the length of a MT and then drawing a region of interest (ROI) around that MT. The ROI was transferred to the Spc105 channel where the total fluorescence intensity of the Spc105-binding variant bound to the MT was measured. Background was corrected by moving the same ROI to a nearby area of the image without MTs. The background signal was subtracted from the Spc105 signal on the MT and divided by the length of the MT to yield a fluorescence intensity per micron of MT.

Live-cell imaging
Metaphase duration measurements were done on living cells, which were previously transfected with C-terminally fluorescent protein

(FP)-tagged Spc105-B, Spc105ΔN, or one of the Spc105ΔN chimeras, seeded onto concanavalin A–coated coverslips. The cells were imaged on a TiE inverted microscope (Nikon) equipped with an iXON3 EMCCD camera (Andor Technology) using a 100 × 1.4 NA Plan Apo violet-corrected (VC) series differential interference contrast objective (Nikon). Metamorph software (Molecular Devices) was used to control the imaging system. Prometaphase cells with one to two misaligned polar chromosomes were identified by scanning the coverslips by eye on the appropriate channel corresponding to the transfected Spc105-FP. The prometaphase cell was then subjected to time-lapse imaging by acquiring images every 2 min to follow the cell from prometaphase until anaphase. Metaphase duration was defined as the time from the last chromosome to biorient, as determined by the position of the sister KTs onto the metaphase plate and an observed increase in centromere stretch, until the separation of sister KTs at anaphase onset. All cells were imaged with the ND4 filter inserted into the light path to limit phototoxicity. The time lapses used to measure metaphase durations were also used to measure K-K distances between the brightest pixels of each sister KT in a bioriented pair.

Stable cell lines expressing the appropriate mCherry-Cry2 constructs were induced for ~16 h with 500 µM CuSO$_4$ the night before Cry2 photo-oligomerization experiments were conducted. Induced cells were seeded onto concanavalin A–treated coverslips, and the media in the imaging chamber was supplemented with 1 µM SiR-tubulin ~30 min before the cells were imaged on the TIRF–spinning-disk system previously described. All time-lapse imaging was conducted such that the mCherry channel (561 nm laser line) was acquired first to visualize the mCherry-Cry2 before optogenetically inducing oligomerization with the 488 nm (blue) laser. To assess MT binding, cells expressing either Spc105-B(1-200)-mCherry-Cry2 (experimental) or mCherry-Cry2 (control) were subjected to a single 1–10 s (varied depending on the expression levels) pulse of 488 nm blue light followed by acquisition of the mCherry and SiR-tubulin (641 nm: far-red) channels at 5–10 s intervals for 1–2 min. To assess PP1-87B localization in relation to Spc105-B(1-200) and MTs, cells coexpressing either Spc105-B(1-200)-mCherry-Cry2 and EGFP-PP1-87B (experimental), Spc105-B(1-200)-mCherry-Cry2 and EGFP (control), or mCherry-Cry2 and EGFP-PP1-87B (control) were subjected to time-lapse imaging of the mCherry and SiR tubulin channels followed by photoactivation and visualization of EGFP using 200 ms 488 nm pulses (exposures) for each time point at 5 s intervals for 1–2 min.

Photoactivation experiments and quantification
For the photoactivation experiments, cells coexpressing PA-GFP-α-tubulin and either Spc105-B-TagRFP-T or Spc105ΔN-EGFP were seeded onto concanavalin A–treated coverslips and imaged with a 100 × 1.4 NA Plan Apo VC oil objective on a Nikon TiE stand outfitted with a Yokogawa X1 spinning disk, a Nikon LUN4 laser launch for imaging, an iXON Ultra 897 EMCCD camera (Andor Technology), a Bruker Galvo Miniscanner, and a second Nikon LUN4 laser launch used for photoactivation. The system was controlled with NIS-Elements software. The methodology for these experiments and analyses was adapted from Cimini et al. (2006). Cells in metaphase were found with fully aligned fluorescent KTs. A rectangular ROI was drawn along one side of the mitotic spindle parallel to the aligned KTs. Cells were first imaged with a 488 nm laser for two frames and were then photoactivated within the ROI with the 405 nm laser for 2 ms under stimulation settings. They were subsequently imaged with 488 nm laser acquisition every 15 s for 10 min. In Spc105-B-TagRFP-T–expressing cells, KTs were found in the red

channel and imaged with 561 and 448 nm for two time points before photoactivation. In the Spc105ΔN-EGFP–expressing cells, KTs were found in the green channel and imaged with 488 nm as previously described. To measure PA-GFP-α-tubulin photobleaching in our imaging conditions, whole cells expressing only PA-GFP-α-tubulin were activated by drawing a circular ROI around the entire cell (n = 10 cells) and subjecting it to identical activation and imaging conditions as were applied to cells in which an ROI within the spindle was used.

PA-GFP turnover was analyzed in NIS Elements (Nikon). First, a rectangular ROI was drawn around the photoactivated region in the spindle and quantified for the Summed Intensity. The region was moved and centered around the photoactivated signal, and the Summed Intensity was rerecorded with each time point to follow the fluxing MTs. The background signal for each time point was the Summed Intensity for an identical ROI placed equidistant from the metaphase plate on the other half of the spindle. The Summed Intensity of the background measurements were subtracted from the Summed Intensity of the photoactivation measurements, and the values were normalized in each cell as a percent change in fluorescence over time with the first time point post-photoactivation set to 100%. The normalized background-corrected fluorescence for each spindle was then corrected for photobleaching using the experimentally defined bleach rate from the whole-cell photoactivation measurements. The mean values of the normalized, background/bleach–corrected PA-GFP signal at each time point from 0 to 300 s (n = 16 Spc105-B–expressing cells, n = 22 Spc105ΔN-expressing cells) were plotted and fitted with a double-exponential curve using the function $F = A1^{(-k1 \times t)} + A2^{(-k2 \times t)}$ to define the MT turnover rates for the kinetochore-microtubule (KT-MTs) and the non–KT-MTs. $A1$ is the percentage of non-KT-MTs, and $A2$ is the percentage of KT-MTs. The turnover rate constants of dissipation for each of these populations are $k1$ and $k2$, respectively, and t is the time following photoactivation (Cimini et al., 2006). The half-lives of each MT population were derived by dividing ln(2) by the rate constant for each population. Curve fitting was performed using KaleidaGraph (Synergy Software). Flux rates were also measured during the analyses by measuring the distance between the center of the photoactivated ROI for control (Spc105-B) and experimental (Spc105ΔN) conditions from t = 0 to t = 300 s.

Statistical analyses
All statistical analyses were done with the PlotsofDifferences web tool at https://huygens.science.uva.nl/PlotsOfDifferences (Goedhart 2019). The reported p values were generated in PlotsofDifferences, which calculates p values using a randomization method that does not rely on any assumptions about the distribution of the data (normal vs. nonnormal).

REFERENCES
Alfieri C, Chang L, Zhang Z, Yang J, Maslen S, Skehel M, Barford D (2016). Molecular basis of APC/C regulation by the spindle assembly checkpoint. Nature 536, 431–436.

Audett MR, Maresca TJ (2020). The whole is greater than the sum of its parts: at the intersection of order, disorder, and kinetochore function. Essays Biochem 64, 349–358.

Bajaj R, Bollen M, Peti W, Page R (2018). KNL1 binding to PP1 and microtubules is mutually exclusive. Structure 26, 1327–1336.e1324.

Boke E, Ruer M, Wühr M, Coughlin M, Lemaitre R, Gygi SP, Alberti S, Drechsel D, Hyman AA, Mitchison TJ (2016). Amyloid-like self-assembly of a cellular compartment. Cell 166, 637–650.

Broad AJ, DeLuca KF, DeLuca JG (2020). Aurora B kinase is recruited to multiple discrete kinetochore and centromere regions in human cells. J Cell Biol 219, e201905144.

Bugaj LJ, Choksi AT, Mesuda CK, Kane RS, Schaffer DV (2013). Optogenetic protein clustering and signaling activation in mammalian cells. Nat Methods 10, 249–252.

Caldas GV, DeLuca KF, DeLuca JG (2013). KNL1 facilitates phosphorylation of outer kinetochore proteins by promoting Aurora B kinase activity. J Cell Biol 203, 957–969.

Cheeseman IM, Anderson S, Jwa M, Green EM, Kang J, Yates JR 3rd, Chan CS, Drubin DG, Barnes G (2002). Phospho-regulation of kinetochore-microtubule attachments by the Aurora kinase Ipl1p. Cell 111, 163–172.

Cheeseman IM, Chappie JS, Wilson-Kubalek EM, Desai A (2006). The conserved KMN network constitutes the core microtubule-binding site of the kinetochore. Cell 127, 983–997.

Cheeseman IM (2014). The kinetochore. Cold Spring Harb Perspect Biol 6, a015826.

Chmátal L, Yang K, Schultz RM, Lampson MA (2015). Spatial regulation of kinetochore microtubule attachments by destabilization at spindle poles in meiosis I. Curr Biol 25, 1835–1841.

Cimini D, Wan X, Hirel CB, Salmon ED (2006). Aurora Kinase Promotes turnover of kinetochore microtubules to reduce chromosome segregation errors. Curr Biol 16, 1711–1718.

Conde C, Osswald M, Barbosa J, Moutinho-Santos T, Pinheiro D, Guimarães S, Matos I, Maiato H, Sunkel CE (2013). Drosophila Polo regulates the spindle assembly checkpoint through Mps1-dependent BubRI phosphorylation. EMBO J 32, 1761–1777.

Cordeiro MH, Smith RJ, Saurin AT (2020). Kinetochore phosphatases suppress autonomous Polo-like kinase 1 activity to control the mitotic checkpoint. J Cell Biol 219, e202002020.

DeLuca JG, Gall WE, Ciferri C, Cimini D, Musacchio A, Salmon ED (2006). Kinetochore microtubule dynamics and attachment stability are regulated by Hec1. Cell 127, 969–982.

DeLuca KF, Meppelink A, Broad AJ, Mick JE, Peersen OB, Pektas S, Lens SMA, DeLuca JG, et al. (2018). Aurora A kinase phosphorylates Hec1 to regulate metaphase kinetochore-microtubule dynamics. J Cell Biol 217, 163–177.

DeLuca KF, Lens SMA, DeLuca JG (2011). Temporal changes in Hec1 phosphorylation control kinetochore–microtubule attachment stability during mitosis. J Cell Sci 124, 622–634.

Desai A, Rybina S, Müller-Reichert T, Shevchenko A, Hyman A, Oegema K (2003). KNL-1 directs assembly of the microtubule binding interface of the kinetochore in C. elegans. Genes Dev 17, 2421–2435.

Eggert US, Kiger AA, Richter C, Perlman ZE, Perrimon N, Mitchison TJ, Field CM (2004). Parallel chemical genetic and genomewide RNAi screens identify cytokinesis inhibitors and targets. PLoS Biol 2, e379.

Espeut J, Cheerambathur DK, Krenning L, Oegema K, Desai A (2012). Microtubule binding by KNL-1 contributes to spindle checkpoint silencing at the kinetochore. J Cell Biol 196, 469–482.

Espeut J, Lara-Gonzalez P, Sassine M, Shiau AK, Desai A, Abrieu A (2015). Natural loss of Mps1 kinase in nematodes uncovers a role for Polo-like kinase 1 in spindle checkpoint initiation. Cell Rep 12, 58–65.

Genin A, Desir J, Lambert N, Biervliet M, Van Der Aa N, Pierquin G, Killian A, Tosi M, Urbina M, Lefort A, et al. (2012). Kinetochore KMN network gene CASC5 mutated in primary microcephaly. Hum Mol Genetics 21, 5306–5317.

Goedhart J (2019). PlotsOfDifferences—a Web App for the Quantitative Comparison of Unpaired Data, https://doi.org/10.1101/578575.

Hayette S, Tigaud I, Vanier A, Martel S, Corbo L, Charrin C, Beillard E, Deleage G, Magaud JP, Rimokh R (2000). AF15q14, a novel partner gene fused to the MLL gene in an acute myeloid leukaemia with a t(11;15)(q23:a14). Oncogene 19, 4446–4450.

Hendrickx A, Beullens M, Ceulemans H, Den Abt T, Van Eynde A, Nicolaescu E, Lesage B, Bollen M (2009). Docking motif-guided mapping of the interactome of protein phosphatase-1. Chem Biol 16, 365–371.

Hoffman DB, Pearson CG, Yen TJ, Howell BJ, Salmon ED (2001). Microtubule-dependent changes in assembly of microtubule motor proteins and mitotic spindle checkpoint proteins at PtK1 kinetochores. Mol Biol Cell 12, 1995–2009.

Howell BJ, Moree B, Farrar EM, Stewart S, Fang G, Salmon ED (2004). Spindle checkpoint protein dynamics at kinetochores in living cells. Curr Biol 14, 953–964.

Ikeda M, Tanaka K (2017). Plk1 bound to Bub1 contributes to spindle assembly checkpoint activity during mitosis. Sci Rep 7, 8794.

Kern DM, Kim T, Rigney M, Hattersley N, Desai A, Cheeseman IM (2015). The outer kinetochore protein KNL-1 contains a defined oligomerization domain in nematodes. Mol Biol Cell 26, 229–237.

Kerres A, Jakopec V, Fleig U (2007). The conserved Spc7 protein is required for spindle integrity and links kinetochore complexes in fission yeast. Mol Biol Cell 18, 2441–2454.

Kiyomitsu T, Obuse C, Yanagida M (2007). Human Blinkin/AF15q14 is required for chromosome alignment and the mitotic checkpoint through direct interaction with Bub1 and BubR1. Dev Cell 13, 663–676.

Krenn V, Wehenkel A, Li X, Santaguida S, Musacchio A (2012). Structural analysis reveals features of the spindle checkpoint kinase Bub1–kinetochore subunit Knl1 interaction. J Cell Biol 196, 451–467.

Krenn V, Overlack K, Primorac I, van Gerwen S, Musacchio A (2014). KI motifs of human Knl1 enhance assembly of comprehensive spindle checkpoint complexes around MELT repeats. Curr Biol 24, 29–39.

Kroschwald S, Maharana S, Simon A (2017). Hexanediol: a chemical probe to investigate the material properties of membrane-less compartments. Matters, DOI: 10.19185/matters.201702000010.

Kuhn J, Dumont S (2017). Spindle assembly checkpoint satisfaction occurs via end-on but not lateral attachments under tension. J Cell Biol 216, 1533–1542.

Lawrimore J, Bloom KS, Salmon ED (2011). Point centromeres contain more than a single centromere-specific Cse4 (CENP-A) nucleosome. J Cell Biol 195, 573–582.

Lénárt F, Petronczki M, Steegmaier M, Di Fiore B, Lipp JJ, Hoffmann M, Rettig WJ, Kraut N, Peters JM (2007). The small-molecule inhibitor BI 2536 reveals novel insights into mitotic roles of polo-like kinase 1. Curr Biol 17, 304–315.

Lince-Faria M, Maffini S, Orr B, Ding Y, Cláudia F, Sunkel CE, Tavares A, Johansen J, Johansen KM, Maiato H (2009). Spatiotemporal control of mitosis by the conserved spindle matrix protein Megator. J Cell Biol 184, 647–657.

Liu D, Vader G, Vromans MJ, Lampson MA, Lens SM (2008). Sensing chromosome bi-orientation by spatial separation of Aurora B kinase from kinetochore substrates. Science 323, 1350–1353.

Liu D, Vleugel M, Backer CB, Hori T, Fukagawa T, Cheeseman IM, Lampson MA (2010). Regulated targeting of protein phosphatase 1 to the outer kinetochore by KNL1 opposes Aurora B kinase. J Cell Biol 188, 809–820.

London N, Ceto S, Ranish JA, Biggins S (2012). Phosphoregulation of Spc105 by Mps1 and PP1 regulates Bub1 localization to kinetochores. Curr Biol 22, 900–906.

Maresca TJ, Salmon ED (2010). Welcome to a new kind of tension: translating kinetochore mechanics into a wait-anaphase signal. J Cell Sci 123(Pt 6), 825–835.

Meadows JC, Shepperd LA, Vanoosthuyse V, Lancaster TC, Sochaj AM, Buttrick GJ, Hardwick KG, Millar JB (2011). Spindle checkpoint silencing requires association of PP1 to both Spc7 and kinesin-8 motors. Dev Cell 20, 739–750.

Moura M, Osswald M, Leça N, Barbosa J, Pereira AJ, Maiato H, Sunkel CE, Conde C, et al. (2017). Protein phosphatase 1 inactivates Mps1 to ensure efficient spindle assembly checkpoint silencing. eLife 6, e25366.

Musacchio A (2015). The molecular biology of spindle assembly checkpoint signaling dynamics. Curr Biol 25, R1002–R1018.

Musacchio A, Desai A (2017). A molecular view of kinetochore assembly and function. Biology 6, 5.

Nakajima H, Toyoshima-Morimoto F, Taniguchi E, Nishida E (2003). Identification of a consensus motif for Plk (Polo-like kinase) phosphorylation reveals Myt1 as a Plk1 substrate. J Biol Chem 278, 25277–25280.

Nasa I, Rusin SF, Kettenbach AN, Moorhead GB (2018). Aurora B opposes PP1 function in mitosis by phosphorylating the conserved PP1-binding RVxF motif in PP1 regulatory proteins. Sci Signal 11, eaai8669.

Nekrasov VS, Smith MA, Peak-Chew S, Kilmartin JV (2003). Interactions between centromere complexes in Saccharomyces cerevisiae. Mol Biol Cell 14, 4931–4946.

Nijenhuis W, Vallardi G, Teixeira A, Kops GJ, Saurin AT (2014). Negative feedback at kinetochores underlies a responsive spindle checkpoint signal. Nat Cell Biol 16, 1257–1266.

Pagliuca C, Draviam VM, Marco E, Sorger PK, De Wulf P (2009). Roles for the conserved Spc105p/Kre28p complex in kinetochore-microtubule binding and the spindle assembly checkpoint. PLoS One 4, e7640.

Petrovic A, Pasqualato S, Dube P, Krenn V, Santaguida S, Cittaro D, Monzani S, Massimiliano L, Keller J, Tarricone A, et al. (2010). The MIS12 complex is a protein interaction hub for outer kinetochore assembly. J Cell Biol 190, 835–852.

Petrovic A, Mosalaganti S, Keller J, Mattiuzzo M, Overlack K, Krenn V, De Antoni A, Wohlgemuth S, Cecatiello V, Pasqualato S, et al. (2014). Modular assembly of RWD domains on the Mis12 complex underlies outer kinetochore organization. Mol Cell 53, 591–605.

Primorac I, Weir JR, Chiroli E, Gross F, Hoffmann I, van Gerwen S, Ciliberto A, Musacchio A (2013). Bub3 reads phosphorylated MELT repeats to promote spindle assembly checkpoint signaling. eLife 2, e01030.

Przewloka MR, Zhang W, Costa P, Archambault V, D'Avino PP, Lilley KS, Laue ED, McAinsh AD, Glover DM (2007). Molecular analysis of core kinetochore composition and assembly in Drosophila melanogaster. PLoS One 2, e478.

Qi H, Rath U, Wang D, Xu YZ, Ding Y, Zhang W, Blacketer MJ, Paddy MR, Girton J, Johansen J, et al. (2004). Megator, an essential coiled-coil protein that localizes to the putative spindle matrix during mitosis in Drosophila. Mol Biol Cell 15, 4854–4865.

Qi H, Rath U, Ding Y, Ji Y, Blacketer MJ, Girton J, Johansen J, Johansen KM (2005). EAST interacts with Megator and localizes to the putative spindle matrix during mitosis in Drosophila. J Cell Biochem 95, 1284–1291.

Rath U, Wang D, Ding Y, Xu YZ, Qi H, Blacketer MJ, Girton J, Johansen J, Johansen KM, et al. (2004). Chromator, a novel and essential chromodomain protein interacts directly with the putative spindle matrix protein skeletor. J Cell Biochem 93, 1033–1047.

Roscioli E, Germanova TE, Smith CA, Embacher PA, Erent M, Thompson AI, Burroughs NJ, McAinsh AD (2020). Ensemble-level organization of human kinetochores and evidence for distinct tension and attachment sensors. Cell Rep 31, 107535.

Rosenberg JS, Cross FR, Funabiki H (2011). KNL1/Spc105 recruits PP1 to silence the spindle assembly checkpoint. Curr Biol 21, 942–947.

Roy B, Verma V, Sim J, Fontan A, Joglekar AP (2019). Delineating the contribution of Spc105-bound PP1 to spindle checkpoint silencing and kinetochore microtubule attachment regulation. J Cell Biol 218, 3926–3942.

Schittenhelm RB, Althoff F, Heidmann S, Lehner CF (2010). Detrimental incorporation of excess Cenp-A/Cid and Cenp-C into Drosophila centromeres is prevented by limiting amounts of the bridging factor Cal1. J Cell Sci 123, 3768–3779.

Schittenhelm RB, Chaleckis R, Lehner CF (2009). Intrakinetochore localization and essential functional domains of Drosophila Spc105. EMBO J 28, 2374–2386.

Shepperd LA, Meadows JC, Sochaj AM, Lancaster TC, Zou J, Buttrick GJ, Rappsilber J, Hardwick KG, Millar JB (2012). Phosphodependent recruitment of Bub1 and Bub3 to Spc7/KNL1 by Mph1 kinase maintains the spindle checkpoint. Curr Biol 22, 891–899.

Shin Y, Berry J, Pannucci N, Haataja MP, Toettcher JE, Brangwynne CP (2017). Spatiotemporal control of intracellular phase transitions using light-activated optoDroplets. Cell 168, 159–171.e14.

Smurnyy Y, Toms AV, Hickson GR, Eck MJ, Eggert US (2010). Binucleine 2, an isoform-specific inhibitor of Drosophila Aurora B kinase, provides insights into the mechanism of cytokinesis. ACS Chem Biol 5, 1015–1020.

Steegmaier M, Hoffmann M, Baum A, Lénárt P, Petronczki M, Krssák M, Gürtler U, Garin-Chesa P, Lieb S, Quant J, et al. (2007). BI 2536, a potent and selective inhibitor of Polo-like kinase 1, inhibits tumor growth in vivo. Curr Biol 17, 316–322.

Sudakin V, Chan GKT, Yen TJ (2001). Checkpoint inhibition of the APC/C in HeLa cells is mediated by a complex of BUBR1, BUB3, CDC20, and MAD2. J Cell Biol 154, 925–936.

Suzuki A, Badger BL, Salmon ED (2015). A quantitative description of Ndc80 complex linkage to human kinetochores. Nat Commun 6, 8161.

Tromer E, Snel B, Kops GJPL (2015). Widespread recurrent patterns of rapid repeat evolution in the kinetochore scaffold KNL1. Genome Biol Evol 7, 2383–2393.

Uchida KSK, Jo M, Nagasaka K, Takahashi M, Shindo N, Shibata K, Tanaka K, Masumoto H, Fukagawa T, Hirota T (2021). Kinetochore stretching-mediated rapid silencing of the spindle-assembly checkpoint required for failsafe chromosome segregation. Curr Biol 31, 1581–1591.e3.

Venkei Z, Przewloka MR, Ladak Y, Albadri S, Sossick A, Juhasz G, Novák B, Glover DM (2012). Spatiotemporal dynamics of Spc105 regulates the assembly of the Drosophila kinetochore. Open Biol 2, 110032.

Vleugel M, Tromer E, Omerzu M, Groenewold V, Nijenhuis W, Snel B, Kops GJ (2013). Arrayed BUB recruitment modules in the kinetochore scaffold KNL1 promote accurate chromosome segregation. J Cell Biol 203, 943–955.

Walker DL, Wang D, Jin Y, Rath U, Wang Y, Johansen J, Johansen KM (2000). Skeletor, a novel chromosomal protein that redistributes during mitosis provides evidence for the formation of a spindle matrix. J Cell Biol 151, 1401–1412.

Wei G, Takimoto M, Yoshida I, Mao PZ, Koya RC, Miura T, Kuzumaki N (1999). Chromosomal assignment of a novel human gene D40. Nucleic Acids Symp Ser 1999, 71–72.

Welburn JP, Vleugel M, Liu D, Yates JR 3rd, Lampson MA, Fukagawa T, Cheeseman IM (2010). Aurora B phosphorylates spatially distinct targets to differentially regulate the kinetochore-microtubule interface. Mol Cell 38, 383–392.

Yamagishi Y, Yang CH, Tanno Y, Watanabe Y (2012). MPS1/Mph1 phosphorylates the kinetochore protein KNL1/Spc7 to recruit SAC components. Nat Cell Biol 14, 746–752.

Yamaguchi M, VanderLinden R, Weissmann F, Qiao R, Dube P, Brown NG, Haselbach D, Zhang W, Sidhu SS, Peters JM, et al. (2016). Cryo-EM of mitotic checkpoint complex-bound APC/C reveals reciprocal and conformational regulation of ubiquitin ligation. Mol Cell 63, 593–607.

Ye AA, Deretic J, Hoel CM, Hinman AW, Cimini D, Welburn JP, Maresca TJ (2015). Aurora A kinase contributes to a pole-based error correction pathway. Curr Biol 25, 1842–1851.

Zhang G, Lischetti T, Nilsson J (2014). A minimal number of MELT repeats supports all the functions of KNL1 in chromosome segregation. J Cell Sci 127, 871–884.